Corrosion Science 59 (2012) 290–306

Contents lists available at SciVerse ScienceDirect

Corrosion Science

journal homepage: www.elsevier.com/locate/corsci

Corrosion susceptibility of Zn–Al alloys with different grains and dendritic microstructures in Nacl solutions

Alicia E. Ares [a,b,*], Liliana M. Gassa [a,c]

[a] Scientific Research Career (CIC) of the National Science Research Council of Argentina (CONICET), Argentina
[b] Faculty of Sciences, National University of Misiones, 1552 Félix de Azara Street, 3300 Posadas-Misiones, Argentina
[c] Research Institute of Theoretical and Applied, Physical Chemistry (INIFTA), Diagonal 113 and 64 Street, 1900 La Plata, Buenos Aires, Argentina

ARTICLE INFO

Article history:
Received 22 August 2011
Accepted 6 March 2012
Available online 14 March 2012

Keywords:
A. Alloy
A. Zinc
A. Aluminium
B. EIS
B. Polarization
C. Passive films

ABSTRACT

The objective of the present research was to study the corrosion susceptibility of different hypoeutectic (Zn–1 wt.%Al, Zn–2 wt.%Al, Zn–3 wt.%Al, Zn–4 wt.%Al) and hypereutectic (Zn–16 wt.%Al, Zn–27 wt.%Al Zn–50 wt.%Al, Zn–96 wt.%Al, and Zn–98 wt.%Al) zinc–aluminium alloys with different grains (columnar, equiaxed and columnar-to-equiaxed transition, CET) and dendritic microstructures in 3% NaCl solution at room temperature.

The corrosion resistance was analyzed by electrochemical impedance spectroscopy (EIS) as a principal technique. The EIS results show that as the aluminium content increases the rate of formation of corrosion products on the alloys also increases. These products appear to have protective features in the light of the results of voltammograms.

1. Introduction

The uses of zinc can be classified into the following categories: (i) coatings, (ii) casting alloys, (iii) alloying element in other alloys, (iv) wrought zinc alloys, (v) zinc oxide and (vi) zinc chemicals. However, nearly half of the zinc produced is used for zinc coatings for corrosion protection of steel structures owing to the high corrosion resistance of zinc in atmospheric and other environments [1].

Zinc-based alloys with high amounts of aluminium (designated as ZA alloys) comprise a family of die casting alloys that have been used in a wide variety of demanding applications. The traditional members of the zinc–aluminium casting alloys are Zn–8 wt.%Al, Zn–12 wt.%Al and Zn–27 wt.%Al alloys. These alloys combine high strength and hardness, good machinability with good bearing properties and wear resistance often superior to standard bronze alloys [2]. Zinc–aluminium alloys are known to possess excellent bearing properties, particularly at high load and low speed. In addition, these alloys have found increasing use for many applications and compete effectively against copper, aluminium and iron-based foundry alloys [3].

The corrosion behaviour of zinc alloys depends on the type of dissolved species, concentration, pH and temperature [4–7]. The presence of various chemical species can change the solubility of the zinc dissolution products by forming complexes with zinc ions, increasing the electrolyte conductivity, modifying the composition, structure and compactness of the corrosion products, forming an insoluble salt film on the surface, providing reactants for the anodic and cathodic reactions, and changing the reaction kinetics through catalytic or inhibitive adsorption.

Electrochemical techniques have been used in a number of studies on the corrosion of zinc in different solutions [2–44]. The kinetics of the zinc electrochemical reaction processes such as dissolution, deposition, hydrogen evolution, oxygen reduction, passivation, and surface film formation, has been the subject of numerous electrochemical studies using different techniques such as dynamic polarization [4,7–21], steady-state polarization [6,10,19,22–31], measurement of current density–time transients [23,32–35], measurement of potential–time transients [23,30,31,33–40], rotating electrode [4,10,15,17,18,27,29,30,41–45] and impedance measurements [4,6,17,19,24,26–29,46,47]. There are only a few research reports on the effects of the microstructure on the corrosion resistance in different processes, and most of them are related to surface preparation and coatings [41,48–57].

Compared with corrosion testing methods such as weight loss measurements, electrochemical techniques are fast and can be used to obtain instantaneous information on a corrosion process, which cannot be provided by weight loss measurements. Also, impedance techniques, along with the linear polarization technique, are the methods most commonly used for determining

* Corresponding author at: Faculty of Sciences, National University of Misiones, 1552 Félix de Azara Street, 3300 Posadas-Misiones, Argentina. Tel.: +54 376 4422186; fax: +54 376 4425414.
E-mail address: aares@fceqyn.unam.edu.ar (A.E. Ares).

0010-938X/$ - see front matter © 2012 Elsevier Ltd. All rights reserved.
http://dx.doi.org/10.1016/j.corsci.2012.03.015

corrosion rates. The electrochemical impedance spectroscopy (EIS) technique is a particularly useful method to study electrode kinetics at the corrosion potential. One advantage of EIS is provided by the small amplitude of the applied voltage perturbation signal, which avoids every irreversible change that may occur in the working electrode, and, at the same time, allows determining the ohmic drop.

Besides, it provides information about the reaction mechanisms, and/or allows evaluating the associated faradaic process parameters such as charge transfer resistance, electrochemical double layer and the resistive and capacitive contributions due to the presence of reaction intermediates [58].

Usually, a corrosion process in a given environment can involve one, two or all three of the following modes: (i) direct dissolution without hindrance from corrosion products, (ii) direct dissolution with hindrance from corrosion products (porous film) and (iii) indirect dissolution through the formation of passive films (compact film), and can change with time from one mode to another [1].

The nature of the corrosion process can be often revealed by an impedance spectrum. Based on the impedance spectra of zinc in deaerated sodium sulphate solutions, Deslouis et al. [6] found that the corrosion resistance is determined by a dissolution and diffusion controlled-process. Cachet et al. [4] found that the presence of HPO_4^{-2} in a Na_2SO_4 solution increases the impedance of the zinc electrode. A strong inhibition of zinc dissolution occurs owing to the formation of a protective surface layer. A Warburg impedance is measured at low frequencies indicating that the corrosion process is controlled by the diffusion of ions through the phosphate passivating layer. For the corrosion of a zinc electrode in bicarbonate solution, Abdel-Aal et al. [22] proposed similar diffusion-controlled processes through a carbonate passive film. Baugh [11] found that the corrosion of a zinc electrode in ClNa at pH 3.8 is a simple charge-transfer dissolution limited by a dissolution-controlled proton reduction, since at high frequencies the Nyquist impedance plot reduces to a semicircle and at low frequencies a Warburg impedance develops. This author also proposed that formation of an oxide film may be involved in the corrosion processes since the double-layer capacitance is considerably smaller around the corrosion potential than in the cathodic region. Deslouis et al. [27] proposed an equivalent circuit for a zinc electrode in 0.5 M Na_2SO_4 [1].

The corrosion of zinc in sulphate or chloride solutions seems to involve a charge-transfer-controlled dissolution process, with a formation of a corrosion product film on the surface and a dissolution process through the film [1,4,6,22,27]. When the zinc surface is free of corrosion products or the corrosion film is of a porous nature, the corrosion process is controlled by charge-transfer-controlled dissolution and/or by the diffusion of the reactants for the cathodic reaction.

When the surface is covered with a passive film, the corrosion process may be controlled by a diffusion process though the film [1].

Among solidification processes, the columnar-to-equiaxed transition (CET) and equiaxed growth still raise issues from the metallurgical point of view and regarding the understanding of the fundamental related physical phenomena [59]. On the other hand, there are relatively few systematic studies in relation to the corrosion behaviour of zinc-based alloys directionally solidified with different macrostructures and in a wide range of compositions. In particular, Osório et al. [60–62] obtained a sharp plane transition, and thus considered columnar and equiaxed macrostructures around the CET zone for the analysis. These authors investigated a number of issues in Zn–Al alloys: (a) the role of macrostructural morphologies in corrosion resistance, i.e., the influence of the columnar and equiaxed macrostructures on the corrosion resistance of aluminium and zinc casting samples; the influence of longitudinal (columnar) and transversal (pseudo-equiaxed) sections of the same sample on the corrosion resistance of both metals; the influence of equiaxed grain size of hot-dip galvanized steel sheets on corrosion resistance [60]; (b) the influence of both the secondary dendrite arm spacings and segregation effects on the corrosion resistance of hypoeutectic and hypereutectic Zn–Al alloys [61]; and (c) the application of electrochemical impedance spectroscopy to investigate the effect of as-cast macrostructures on the corrosion resistance of hypereutectic Zn–Al alloys [62].

In previous works, we correlated the effect of several parameters, like thermal, metallurgical and electrochemical parameters, on the CET macrostructure in Zn–4 wt.%Al, Zn–16 wt.%Al and Zn–27 wt.%Al alloys [63].

The grain and dendrite morphologies play an important role in the corrosion behaviour of metallic materials. Grain boundary-dependent properties such as fracture and intergranular corrosion have been found to be strongly dependent on the crystallographic nature of the grain boundaries [64].

Intergranular corrosion of zinc alloys has been reported to be a serious problem for die-cast alloys used in hot water and warm humid atmospheres, and has been associated with the presence of aluminium along with certain impurities such as lead and cadmium in the alloys [1,65–67].

Dendrite morphology can be observed during metal casting and is characterized by the microstructure parameters. A convenient method widely used to determine the effect of dendrite morphology on solidification is to measure dendrite arm spacing (λ). Numerous solidification studies have characterized the primary dendrite arm spacing (λ_1), secondary dendrite arm spacing (λ_2) and tertiary dendrite arm spacing (λ_3) as a function of the alloy solute concentration, growth rate and temperature gradient ahead of the microscopic solidification front [68–79].

Calculating and predicting the dendrite arm spacing is very important because it has been demonstrated that λ_2 has a significant effect on the mechanical properties of the metal [80–86]. However, the state-of-the-art indicates that the effects of the grain size, dendrite arm spacing and solute redistribution on the corrosion resistance of metallic alloys are not very clear.

The aim of this work was to investigate the susceptibility to corrosion of hypoeutectic and hypereutectic zinc–aluminium alloys with different grain sizes, dendrite arm spacings and solute redistribution phenomena, in 3% NaCl solution at room temperature, using electrochemical impedance spectroscopy as a principal technique and correlating the variation in EIS parameters with grain and dendrite morphologies (metallurgical parameters).

2. Materials and methods

2.1. Directional solidification process and metallography

Zinc–aluminium (ZA) alloys of different compositions were prepared with zinc and aluminium of commercial grade. Their chemical compositions are shown in Table 1.

The samples were directionally solidified in Pyrex molds 16 mm in diameter and 200 mm in length and then melted and solidified directionally upwards in an experimental set-up described elsewhere [87]. The experimental set-up was designed in such a way that the heat was extracted only through the bottom, promoting upward directional solidification to obtain the CET (see Figs. 1 and 2).

In order to reveal the macrostructure (type and size of grains), after solidification, the samples were cut in the axial direction, ground, polished and etched using concentrated hydrochloric acid for 3 s at room temperature. This was followed by rinsing and

Table 1
Chemical composition of the Zn and Al ingots used to prepare the ZA alloys directionally solidified.

Element	Zn	Fe	Si	Pb	Others
Zn sample					
Weight percent	99.98 ± 0.2	0.010 ± 0.001	0.006 ± 0.0001	0.004 ± 0.001	<0.001 ± 0.0001
Al sample					
Element	Al	Fe	Si	Pb	Others
Weight percent	99.94 ± 0.2	0.028 ± 0.001	0.031 ± 0.001	0.001 ± 0.0001	<0.001 ± 0.0001

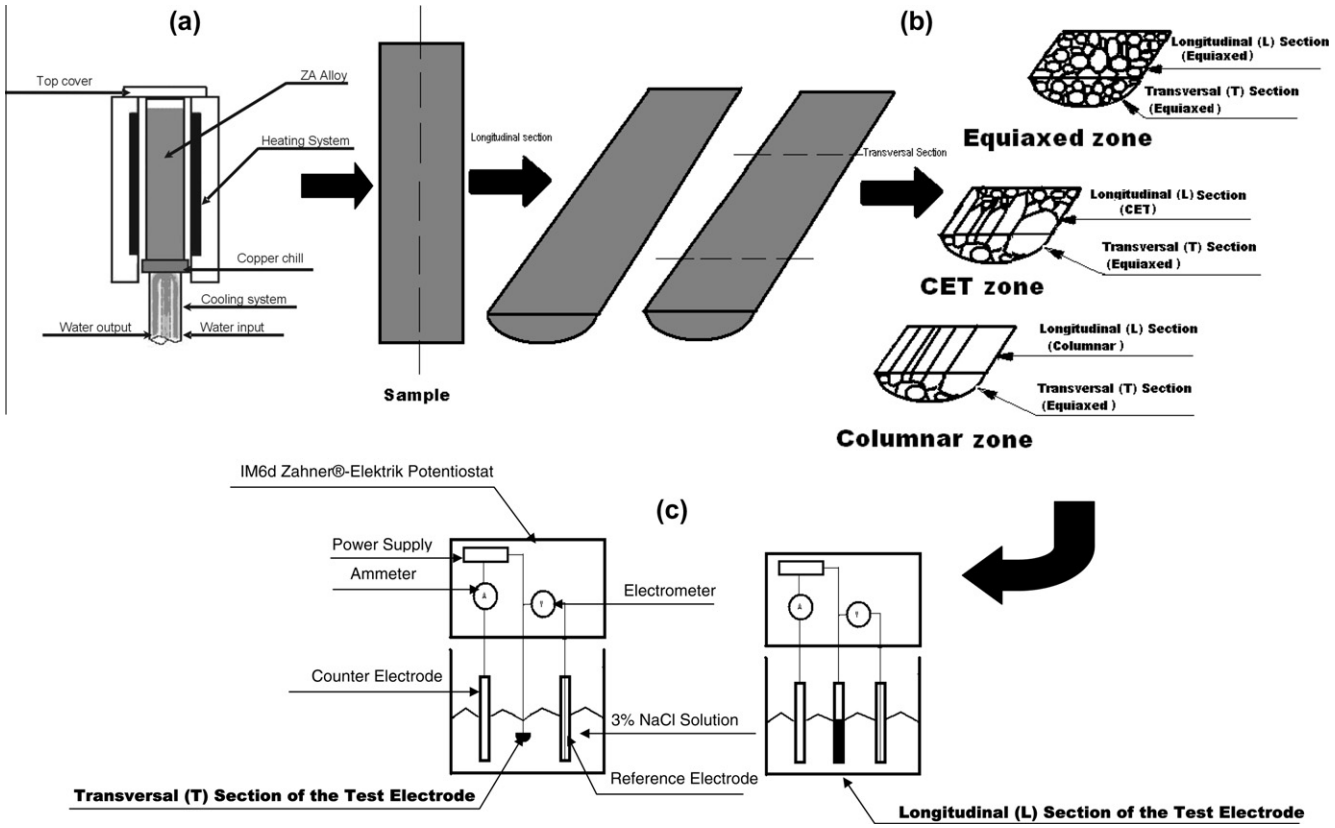

Fig. 1. Schematic representation of: (a) the vertical upward solidification system, (b) the longitudinal (L) and transversal (T) sections of the cylindrical sample and (c) the position of the longitudinal and transversal sections as a test electrode in the cell kit.

wiping off the resulting black deposit. To examine the microstructures (dendrites) the samples were etched with a mix containing chromic acid (50 g Cr_2O_3; 4 g Na_2SO_4 in 100 ml of water) for 10 s at room temperature [88]. Fig. 2 shows typical longitudinal macrostructures (a)–(e) and microstructures (f)–(k) of different areas of the same sample.

The grain size (G_s) and secondary dendritic arm spacing (λ_2) were measured at each location using an Arcano® metallographic microscope and the SIS image-analysis software. The secondary dendritic arm spacings were measured by counting the number of branches along a line of known length [89]. The mean value of λ_2 was calculated from 15 measurements in each zone of the samples (columnar, CET and equiaxed).

To measure the equiaxed grain size from the CET zone to the top, each sample was divided into equal intervals. The average diameter of equiaxed grains was calculated in each interval of approximately 10 mm, according to the ASTM 112-96 standard norm [89]. The columnar region was divided into similar size intervals and the width and length of the columnar grains were measured directly from the samples.

The position of the CET in the macrostructures of the samples was located by visual observation and optical microscopy and the distance from the chill zone of the sample was measured with a ruler.

It is noted in Fig. 2 that the CET is not sharp, showing an area where some equiaxed grains co-exist with columnar grains. The following alloys were selected for the present study: (a) the hypoeutectic alloys Zn–1 wt.%Al, Zn–2 wt.%Al, Zn–3 wt.%Al and Zn–4 wt.%Al, and (b) the hypereutectic alloys Zn–16 wt.%Al, Zn–27 wt.%Al, Zn–50 wt.%Al, Zn–98 wt.%Al and Zn–96 wt.%Al.

2.2. Corrosion tests

For the electrochemical tests, samples of 20 mm in length of each zone and for each concentration were prepared as test electrodes (see Fig. 1). The electrodes were polished with grit paper in decreasing size from # 80 to # 1200 followed by 0.3 μm alumina powder. Finally they were rinsed with twice-distilled water and dried by natural air flow.

All the electrochemical tests were conducted in 3% NaCl solution (pH 5,5) at room temperature (25 °C) using an IM6d Zahner®-Elektrik potentiostat coupled to a frequency analyzer system. A conventional three-compartment glass electrochemical cell with its compartments separated by ceramic diaphragms was used.

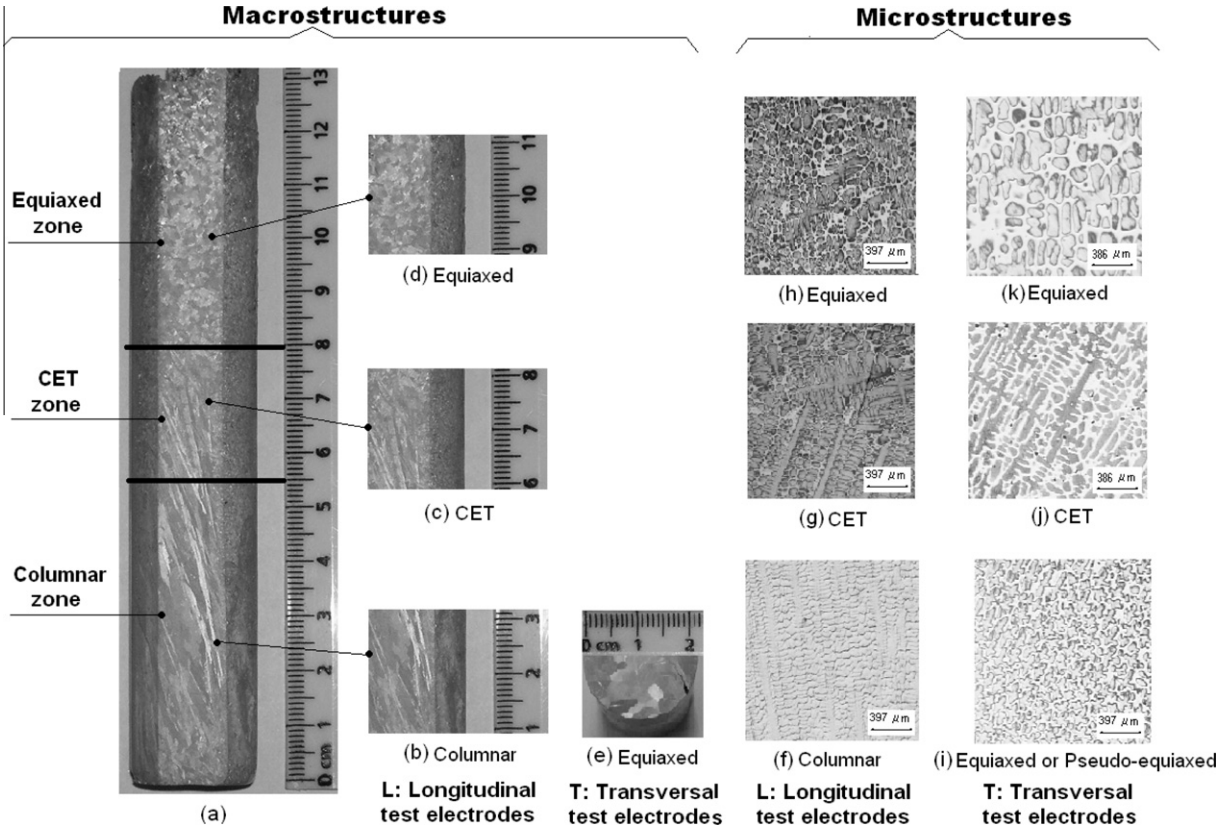

Fig. 2. (a) Macrostructure of the Zn–4 wt.%Al alloy. (b–d) Longitudinal test electrodes of different grain structures. (e) Transversal test electrode of the columnar zone of the sample showing the equiaxed or pseudo-equiaxed grains. (f–h) Different types of dendrites in the longitudinal test electrodes. (i–k) Equiaxed or pseudo-equiaxed dendrites in the transversal electrodes.

The test electrodes (area ≅ 2 cm^2) consisted of longitudinal (L) or transversal (T) sections of the Zn–Al ingots (see Fig. 1) and were positioned at the glass corrosion cell kit (leaving a rectangular area in the case of the longitudinal sections or a semi-cylindrical area in the case of the transversal sections in contact with the electrolyte). The potential of the test electrode was measured and referred to a saturated calomel reference electrode (0.242 V vs. SHE), provided with a Luggin capillary tip. A large-area Pt sheet was used as a counterelectrode.

Voltammograms were run between preset cathodic (open circuit potential ≈−1.500 V) and anodic ($E_{s,a}$ = −0.700 V) switching potentials at potential sweep rates (v) of 0.002 V s^{-1}. Impedance spectra were obtained in the frequency range of 10^{-3} Hz ⩽ f ⩽ 10^5 Hz an open circuit potential and the potential amplitude was set to 5 mV. The EIS measurements began after the current reached a steady state value (≅20 min).

For comparison purposes, experiments using pure metals and aluminium-based alloys with different structures were conducted under the same experimental conditions. All the EIS experiments were carried out in triplicate and the average values and graphical outputs are reported.

3. Results

3.1. Microstructures formed in hypoeutectic and hypereutectic alloys during directional solidification

According to the Zn–Al phase diagram (Fig. 3) the phase formed at 418 °C is β (Zn) and liquid (L) until 382 °C. Below this temperature, part of β (Zn) forms the γ phase (ZnAl) + β (Zn), until 275 °C, when the eutectoid transformation γ (ZnAl) → α (Al) + β (Zn) occurs. Below 275 °C, β (primary, rich in Zn) + eutectoid (α + β) is formed. However, our directional solidification is a non-equilibrium solidification, and then high-temperature phases can be retained towards room temperature. Fig. 4(a) shows the microstructure of the Zn–1 wt.%Al alloy, in the equiaxed zone, showing the β (Zn) dendrites without the formation of interdendritic zone.

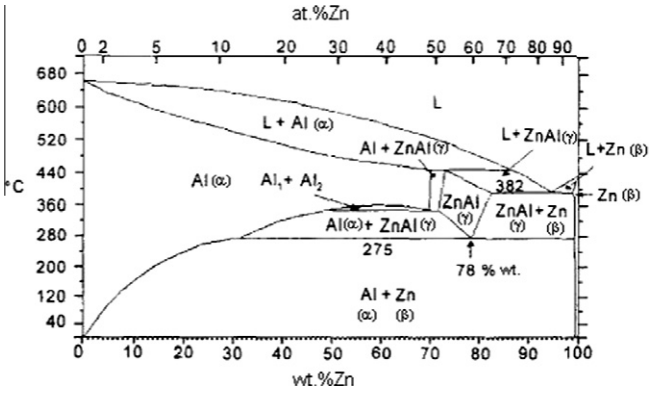

Fig. 3. Zn–Al phase diagram [89].

In the case of the hypoeutectic alloys Zn–2 wt.%Al, Zn–3 wt.%Al and Zn–4 wt.%Al, at approximately 416 °C, the β (Zn) phase + liquid (L) is formed until 382 °C, when the eutectic transformation L → β (Zn) + γγ (ZnAl) occurs. Below 382 °C, β (Zn) phase + eutectic (β (Zn) + γ (ZnAl)) is formed until 275 °C, when the eutectic transformation γ (ZnAl) → α (Al) + β (Zn) occurs. Below 275 °C, the β (primary, rich in Zn) + eutectoid (α + β) is formed.

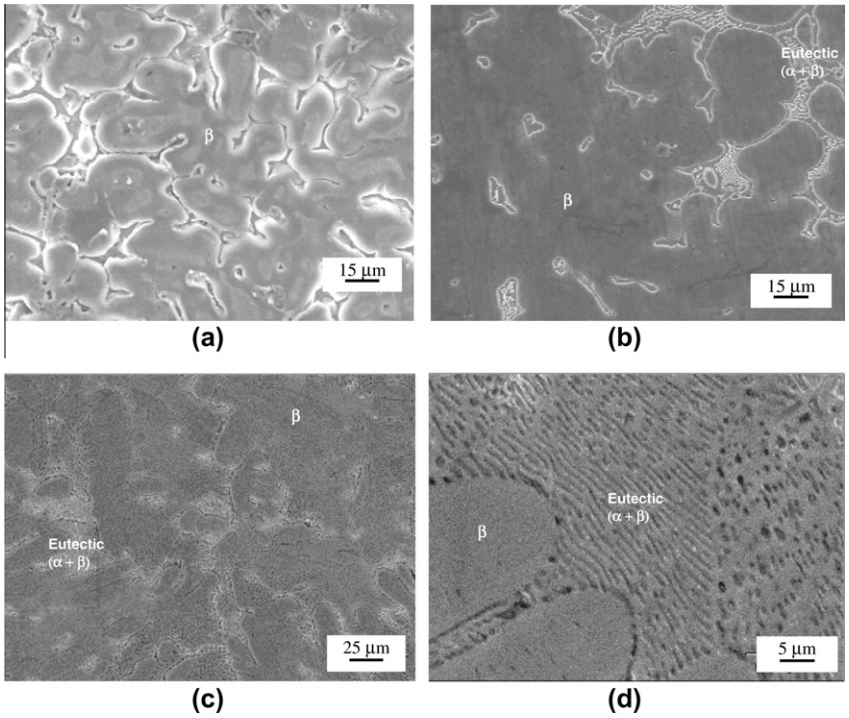

Fig. 4. Typical morphology of hypoeutectic Zn–Al alloys: (a) Zn–1 wt.%Al alloy showing the β (Zn) dendrites without the formation of interdendritic zone. (b) Zn–2 wt.%Al alloy showing the β (Zn) dendrites and a small interdendritic zone with eutectic formation. (c) Zn–3 wt.%Al alloy showing the β (Zn) dendrites. (d) Zn–4 wt.%Al alloy showing the eutectic lamellar morphology (β + α).

From Zn–2 wt.%Al to Zn–4 wt.%Al alloys, the eutectic phase (inter-dendritic region) formed increases at expense of the β (Zn) (see Table 2 and Fig. 4(b)–(d)).

In the case of the hypereutectic alloy Zn–16 wt.%Al, α (Al) + liquid (L) is formed above 430 °C. Below this temperature, the α (Al) phase becomes enriched in Zn, forming the γ (ZnAl) phase until 382 °C.

Below 430 °C, the γ (ZnAl) phase increases the concentration of Zn and the remaining liquid solidifies with the eutectic composition until 382 °C., the γ phase becomes impoverished in Zn and the β phase (in the eutectic phase) is slightly enriched in Zn until 275 °C. At 275 °C, the eutectoid formation γ (ZnAl) → α (Al) + β (Zn) occurs. Between 275 °C and room temperature, β (primary, rich in Zn) + eutectoid (α + β) is formed.

In the case of the Zn–27 wt.%Al alloy, α (Al) + liquid (L) is formed above 430 °C. Below this temperature, the γ phase (ZnAl) is formed until 315 °C. At 315 °C, the γ phase separates into α and γ until 275 °C, when the eutectoid transformation γ (ZnAl) → α (Al) + β (Zn) occurs. Below 275 °C, α (rich in Al) + (α + β) is formed.

Table 2
Solid and liquid fractions of hypoeutectic and hypereutectic ZA alloys.

Alloy	f_s (Dendritic region) (%)	f_l (Inter-dendritic region) (%)
Hypoeutectic alloys ($k = C_S/C_L = 0.20$)		
Zn–1 wt.%Al	87	13
Zn–2 wt.%Al	68	32
Zn–3 wt.%Al	47	53
Zn–4 wt.%Al	25	75
Hypereutectic alloys ($k = C_S/C_L = 3.44$)		
Zn–16 wt.%Al	12	88
Zn–27 wt.%Al	45	55
Zn–50 wt.%Al	60	40

Finally, during solidification of Zn–50 wt.%Al, the formation of α (Al) + liquid (L) occurs from 570 to 470 °C. Below 470 °C, α (rich in Al) is formed until 345 °C, when the α phase separates in (α + γ) until 275 °C. At this temperature, the eutectoid transformation γ (ZnAl) → α (Al) + β (Zn) occurs.

Below 275 °C, β (primary, rich in Zn) + eutectoid (α + β) is formed.

From Zn–16 wt.%Al to Zn–50 wt.%Al alloys, the eutectic phase (inter-dendritic region) formed decreases at expense of the α (Al) (Table 2 and Fig. 5(a)–(c)).

Finally, in the case of Zn–96 wt.%Al and Zn–98 wt.%Al, the formation of α (Al) + liquid (L) occurs at 657 and 652 °C, respectively, until 650 and 647 °C correspondingly. Then, the α (Al) phase is formed only until room temperature (Fig. 5(e) and (f)).

The typical microstructures of hypereutectic zinc–aluminium alloys is presented in Fig. 5 for (a) Zn–16 wt.%Al, (b) Zn–27 wt.%Al and (c) Zn–50 wt.%Al alloys. The micrograph shows the α (Al) dendrites with the (α + β) eutectoid phase in the interdendritic region, which decreases from (a) to (c) as the Al content in the alloy increases.

The solidification microstructure of the Zn–27 wt.%Al and Zn–50 wt.%Al alloys presented a dendritic structure consisting of α primary dendrites rich in aluminium, evidenced by the EDXA shown in Fig. 5(b)–(d). The (α + β) eutectoid is formed from α dendrites and the peritectic through a transformation at 275 °C, following the Al–Zn phase diagram (Fig. 3) and formed during the final stage of solidification. This (α + β) eutectoid has the typical plate-like shape of α and β sheets. In addition, a standard and finer eutectic structure is observed at the edge of the dendrites of the matrix.

3.2. Evolution of metallurgical parameters (secondary dendritic arm spacing and grain size) with directional solidification

The typical EDXA micrograph of the hypoeutectic and hypereutectic Zn–Al alloys studied is presented in Fig. 6. It is possible to

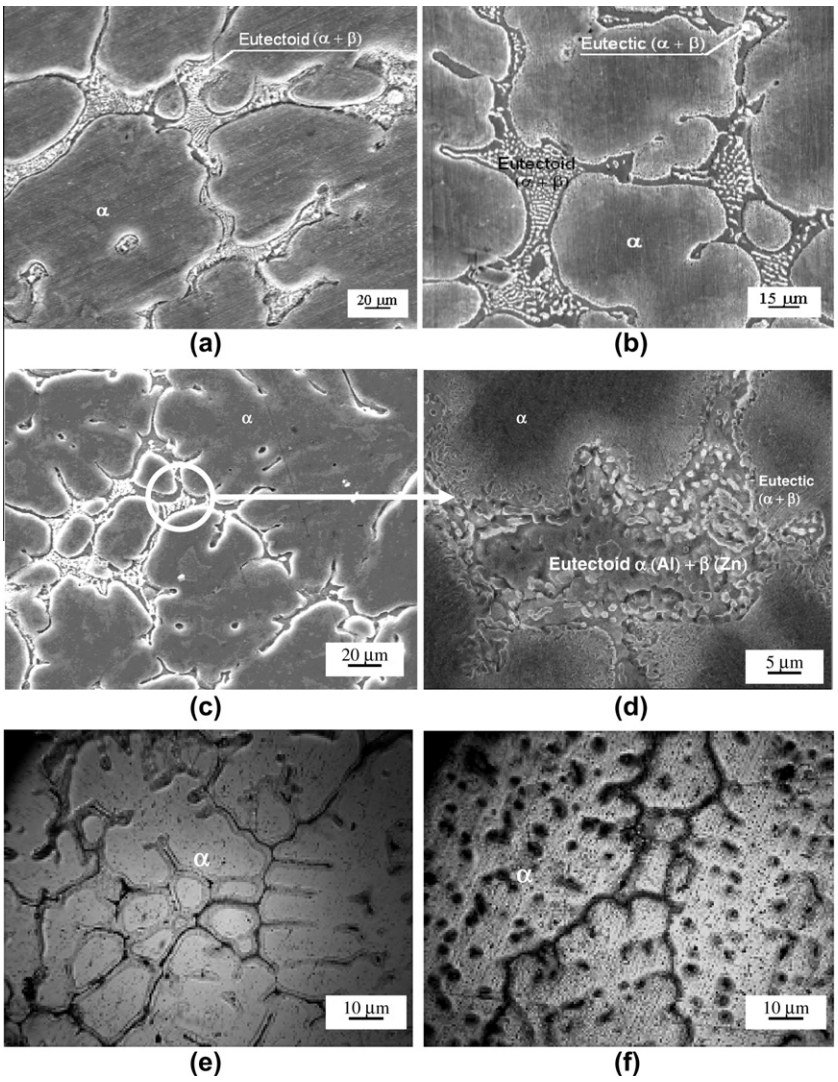

Fig. 5. Typical morphology of hypereutectic Zn–Al alloys: (a) Zn–16 wt.%Al, (b) Zn–27 wt.%Al and (c) Zn–50 wt.%Al. The micrographs show the α (Al) dendrites with the (α + β) eutectoid phase. The eutectoid phase increases from (a) to (c) as the Al content in the alloy increases. (e) Zn–96 wt.%Al and (f) Zn–98 wt.%Al alloys: the micrographs in both cases show the α (Al) dendrites.

observe that the dendritic matrix of Zn–4 wt.%Al is Zn-rich (β phase) (Fig. 6(a)), whereas the interdendritic region, which is the eutectic (α + β) phase, is Al-rich (Fig. 6(b)).

The microstructure of the hypereutectic Zn–27 wt.%Al alloy is presented in Fig. 7. The dark region in Fig. 7(a) is the dendritic matrix, which is Al-rich (α phase), whereas the light inter-dendritic region, which includes the eutectic and eutectoid phases, is Zn-rich (Fig. 7(b)). This analysis demonstrates that the solute redistribution phenomenon for Zn–Al hypereutectic alloys is opposed to the solute distribution of hypoeutectic alloys.

To analyze the evolution of secondary dendrite arm spacing (λ_2) in the microstructure with the distance from the caloric extraction surface (bottom of the sample), we plotted Fig. 8(a) and (b) for all hypoeutectic (Zn–1 wt.%Al, Zn–2 wt.%Al, Zn–3 wt.%Al and Zn–4 wt.%Al) and hypereutectic (Zn–16 wt.%Al, Zn–27 wt.%Al and Zn–50 wt.%Al) alloys. These plots show that λ_2 increases from the columnar (bottom) to the equiaxed (top) zone of the samples because the heat extraction and cooling rate are higher during the columnar than the equiaxed growth, producing a shorter solidification time.

Fig. 8(a) also shows that λ_2 decreases from 1 wt.%Al to 4 wt.%Al, which is expected for the higher increase in the solute at dendrite interface arms, which is predicted by models [83]. In addition, there might be a difference in the solidification time between the experiments. In contrast, in the case of hypereutectic alloys, it is observed than λ_2 increases from 16 wt.%Al to 50 wt.%Al (Fig. 8(b)).

The evolution of grain size (G_s) in the macrostructure with distance from the bottom of the sample is presented in Fig. 9(a) and (b). The size of the equiaxed grains for the Zn–1 wt.%Al sample is 0.15 cm in the transition region and then starts to increase monotonically up to a value of 0.45 cm at the end of the sample. In the case of the width of the columnar grains, it is observed that the size increases from 0.2 cm in the entire columnar zone to 0.38 cm at the end of the transition region (Fig. 9(a)).

A similar analysis was performed for all solidification experiments, as shown in Fig. 9 for other alloy concentrations. In the transition zone, the size of the equiaxed grains is smaller than the width of the columnar grains (the black points in the figures correspond to the measurements of the size of the columnar and equiaxed dendrites in the CET zone). However, in all cases, the size increases after the transition. At the end of solidification, the size of equiaxed grains also reaches a maximum value.

Fig. 9 shows that the grain size in the Zn–2 wt.%Al sample increases from 0.18 to 0.27 cm in the columnar zone and from 0.14 to 0.38 cm in the equiaxed zone. In the Zn–3 wt.%Al alloy, the grain size is between 0.17 and 0.27 cm in the columnar zone and between

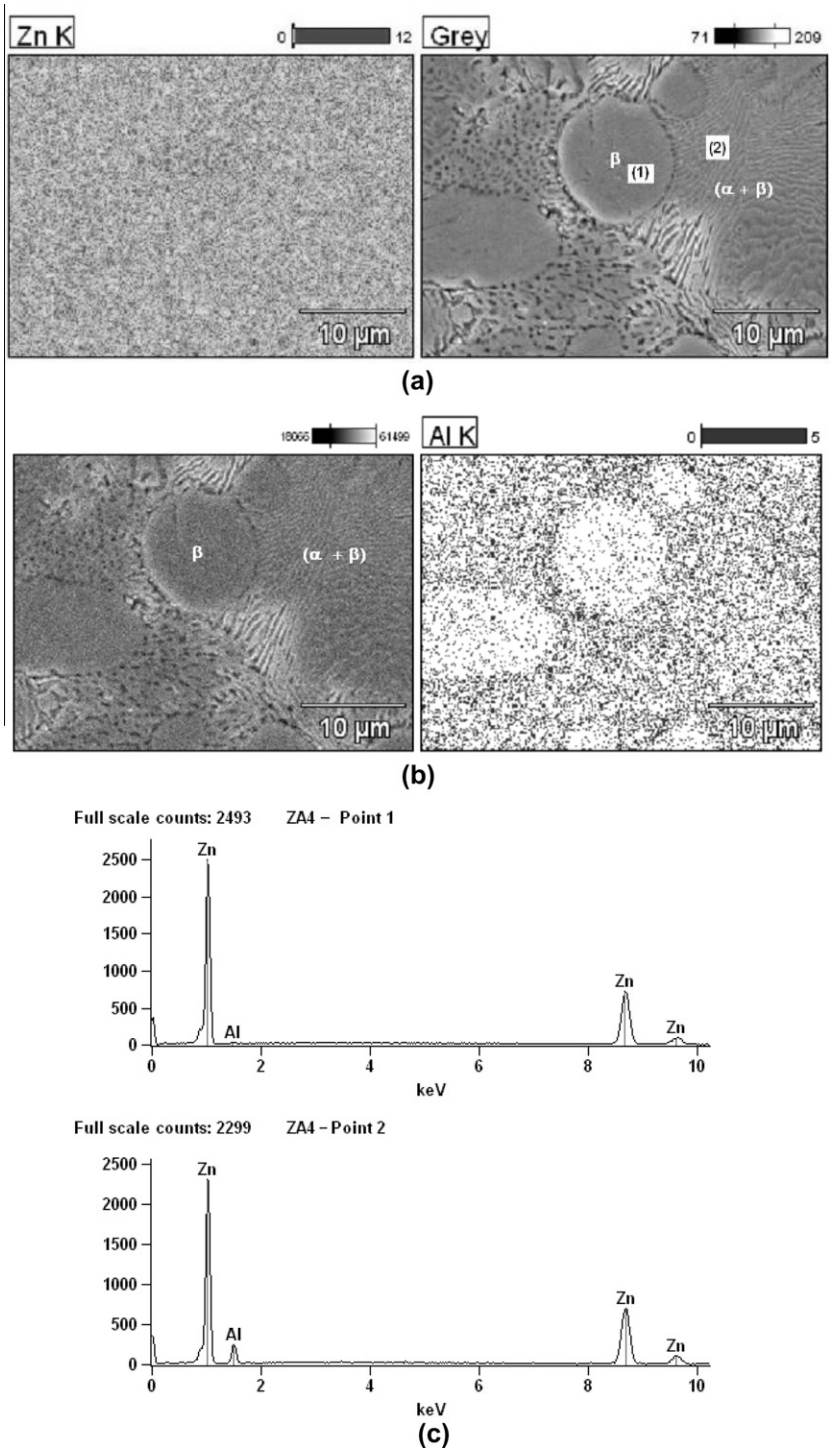

Fig. 6. (a) and (b) Scanning electron microscopy with (c) EDXA analysis of Zn–4 wt.%Al alloy showing the distribution of elements. The Zn is distributed in the β dendrites and in the eutectic phase. α (Al) is present in the eutectic phase (α + β).

0.12 and 0.35 cm in the equiaxed zone. Finally, for the Zn–4 wt.%Al alloy, the size increases from 0.13 to 0.32 cm (columnar zone) and from 0.08 to 0.22 cm (equiaxed zone). The size of the grains in the three zones (columnar, CET and equiaxed) decreases from the Zn–1 wt.%Al to the Zn–4 wt.%Al alloy for the hypoeutectic alloys.

Also, the G_s for hypereutectic alloys are smaller than those for the hypoeutectic alloys and decrease in size from Zn–16 wt.%Al to Zn–50 wt.%Al (Fig. 9(b)).

This analysis of the sizes of the grains shows that the coarser equiaxed grains are produced at the top of the samples rather than in the middle, where the CET normally occurs and that the finer columnar grains are located at the bottom of the samples. Finally, the grain sizes become finer when the concentration of aluminium in the alloys increases.

3.3. Voltammetric data

During the anodic potential scanning, the voltammogram of equiaxed zinc shows that the current is practically zero until it

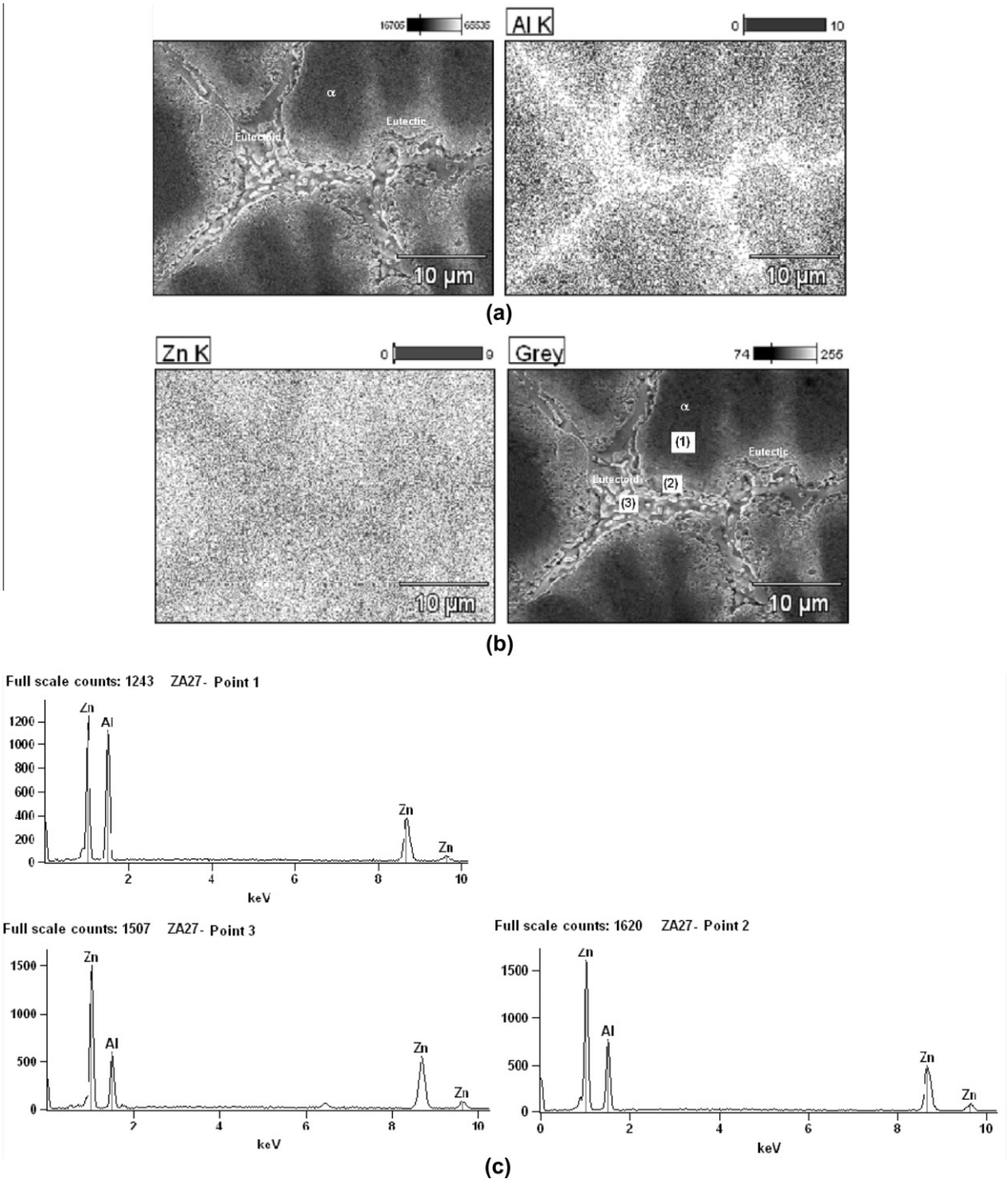

Fig. 7. (a) and (b) Scanning electron microscopy with (c) EDXA analysis of Zn–27 wt.%Al alloy showing the distribution of elements. The distribution of α (Al) is in dendrites and eutectic and eutectoid phases. The Zn is distributed principally in the eutectoid and eutectic phases.

reaches a potential of −1 V, where the current rises sharply, starting the active dissolution of the metal (Fig. 10(a)).

The negative potential scan shows a hysteresis loop, suggesting that this increase in the current was due to the start of a process of pitting, and two cathodic current peaks at about −1.2 and −1.3 V (called C_1 and C_2). These peaks could be associated with the reduction of $Zn(OH)_2$ and ZnO, respectively [1,90]. The composition of corrosion products formed on the zinc surface may be not uniformly distributed. The different compositions and microstructures of the films formed can explain the difference between the voltammetric profiles obtained for the different alloys and those reported in the literature [60–62].

For example, only one peak appears in the case of the columnar zinc (not shown here). When aluminium is added to the alloy, the definition of the reduction peaks is not clear, although the C_2 peak is dominant (Fig. 10(b) and (c)).

In the case of the alloys, the values of the anodic currents are similar for the same Al concentration, independently of the microstructure, and the most important difference is observed in the distribution of the cathodic current peaks, which indicates the

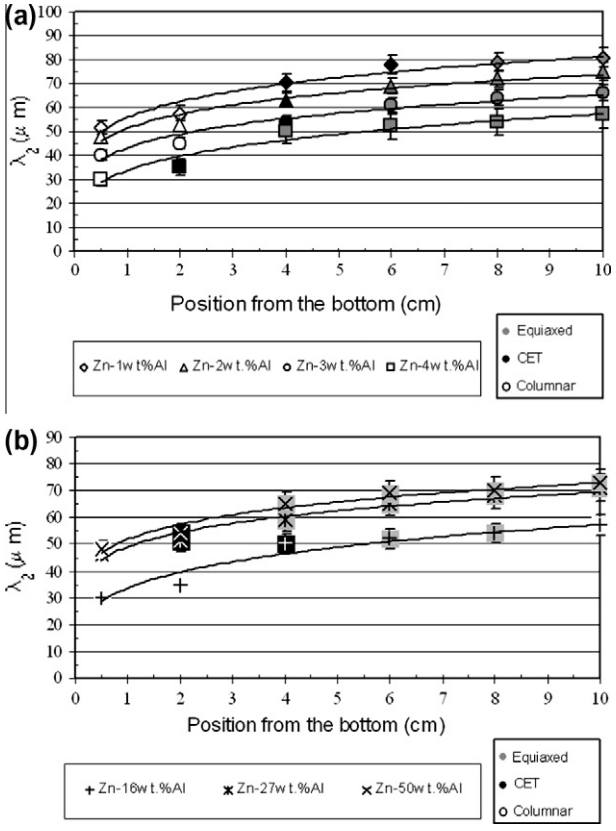

Fig. 8. Secondary dendrite arm spacing (λ_2) as a function of distance from the bottom of the samples. (a) Hypoeutectic alloys and (b) Hypereutectic Zn–Al alloys.

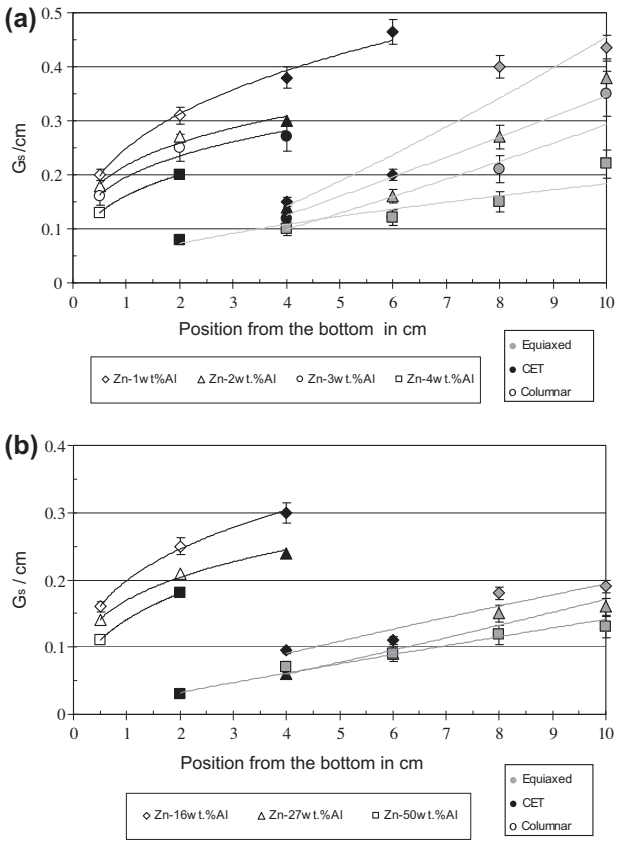

Fig. 9. Grain size (G_s) as a function of distance from the bottom of the samples. (a) Hypoeutectic alloys and (b) Hypereutectic Zn–Al alloys.

different characteristics of the films formed during the anodic scan. These results can be attributed to the aggressive/depassivating action of Cl^- anions [91]. At present, the mechanism of film formation is still uncertain.

For the case of CET, profiles are more complex, because the proportion of one or other type of grains (columnar or equiaxed) can vary from sample to sample (Fig. 10(d)).

Also, as the concentration of Al increases, the voltammetric profile of the different structures tends towards the response of pure aluminium and aluminium alloys with low zinc content (Fig. 10(e)), although the current values remain one order of magnitude lower than those obtained for the pure metal.

The complex distribution of the current of the peaks in the potential/current density response of the alloys is also evident when comparing the voltammetric responses of the longitudinal and transverse sections of the samples (Fig. 10(f)). As the Al concentration increases, the reduction current decreases to about half, indicating that the passive layer formed on the material is more protective, an effect that is accelerated in the transversal sections. Now the grain structure in a polycrystalline zinc alloy has preferred orientations depending on the casting and mechanical working conditions, i.e., for cast products the ⟨0001⟩ direction is perpendicular to the axis of the cast columnar crystals [92]. Thus, in the transversal sections, the grains grow in more favourable directions than in the longitudinal sections to promote the formation of a film with more protective characteristics.

This different contribution of the peaks in the voltammograms gives rise to surface layers with different corrosion products, as shown in the micrographs of Fig. 11, where samples with a higher proportion of aluminium (hypereutectic alloys) show the formation of a thicker layer of corrosion products, see Fig. 11(g)–(i) for Zn–16 wt.%Al, Zn–27 wt.%Al, Zn–50 wt.%Al, Zn–96 wt.%Al and Zn–98 wt.%Al show not only the formation of corrosion products on the surface, but also the presence of porosity (Fig. 11(i)).

3.4. Electrochemical impedance spectroscopy data

Fig. 12 shows the impedance spectra in Nyquist format for the longitudinal section of hypoeutectic (Fig. 12(a) and (c)) and hypereutectic (Fig. 12(b) and (d)) Zn–Al alloys. The diameter of the capacitive semicircle of the Nyquist plot is closely related to the corrosion rate. All the diagrams show one capacitive time constant at high frequencies and a non-well defined time constant at low frequencies, probably associated with diffusion processes also reported in the literature [27,93]. The response of the transversal samples is similar to that of the longitudinal equiaxed samples, since, as shown in Fig. 1, the transversal section left exposed mainly an equiaxed or pseudo-equiaxed microstructure.

In some cases, the shape of the Nyquist diagrams for CET morphology resembles that of those with equiaxed grains and of those with columnar grains, depending on the relative amount of each phase in the CET morphology, which in turn depends on the region where the specimen was obtained.

The Nyquist diagrams for the cross-section for all structures of the different alloys (not shown here) are similar to those obtained for the equiaxed structure, since, as shown in Fig. 6(c) and (d), the cross-section is essentially equiaxed (or pseudo-equiaxed).

The equivalent circuit used to fit experimental data is presented in Fig. 13.

The whole set of experimental impedance spectra can be discussed according to the following total transfer function.

$$Z_t(jw) = R_\Omega + Z \quad (1)$$

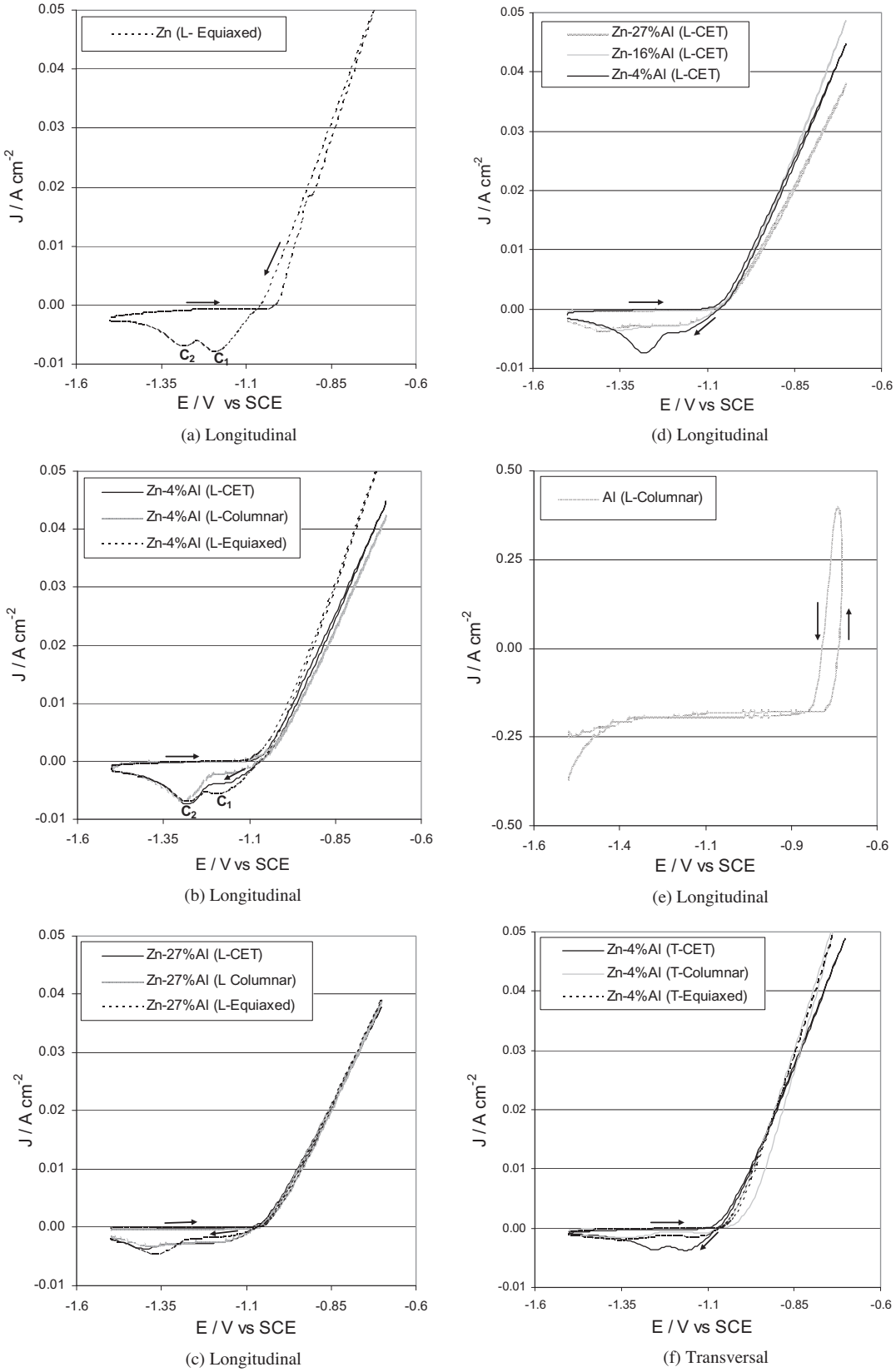

Fig. 10. Voltammograms of longitudinal (L) electrodes of (a) pure $Zn_{Equiaxed}$, (b) Zn–4 wt.%Al alloy with different types of grains (columnar, CET and equiaxed), (c) Zn–27 wt.%Al alloy with different types of grains (columnar, CET and equiaxed), (d) CET grains for different alloys and (e) pure $Al_{Columnar}$. (f) Voltammograms of transversal (T) electrodes of Zn–4 wt.%Al alloy with different types of grains (columnar, CET and equiaxed).

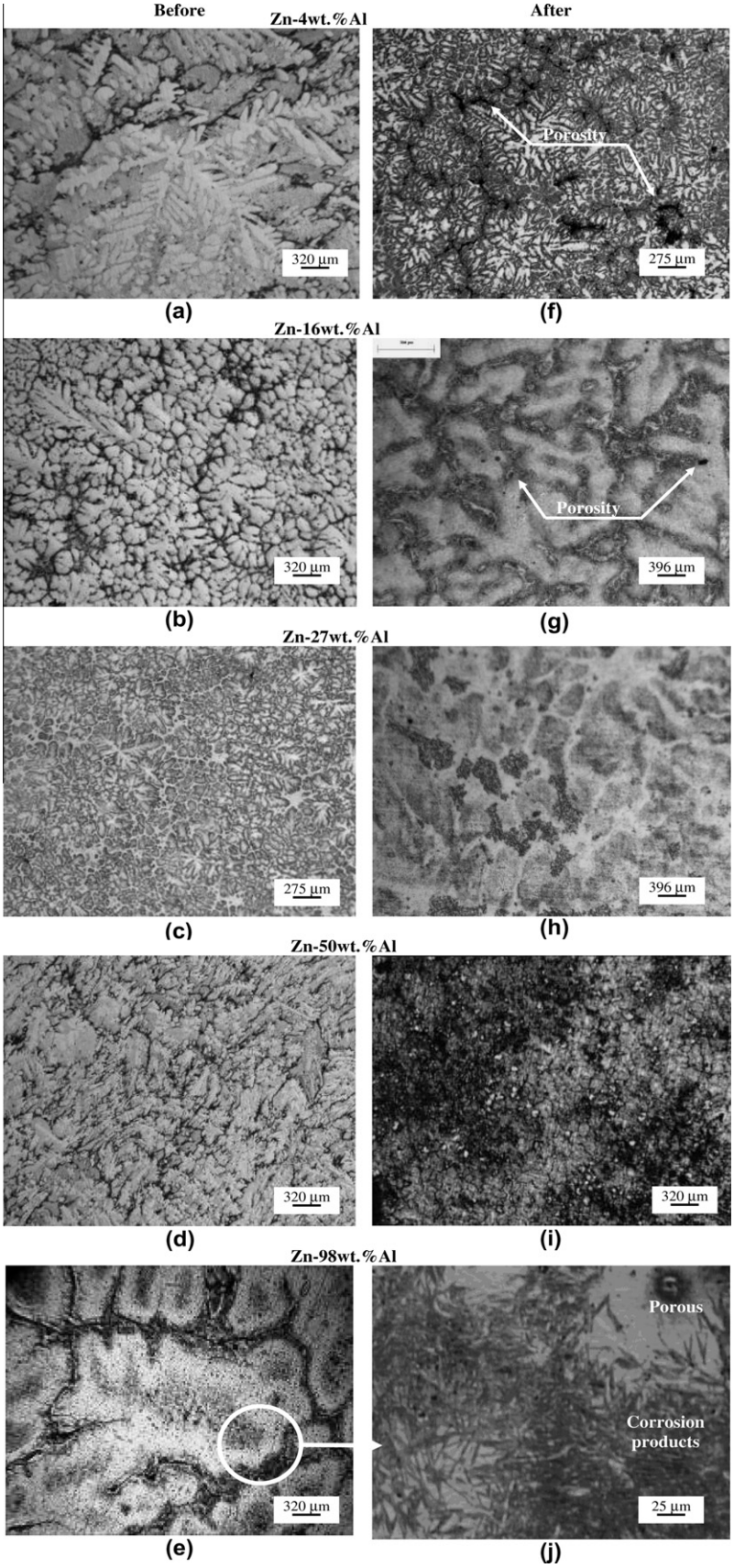

Fig. 11. Micrographs of different alloy samples before (a)–(e) and after (f)–(j) corrosion tests.

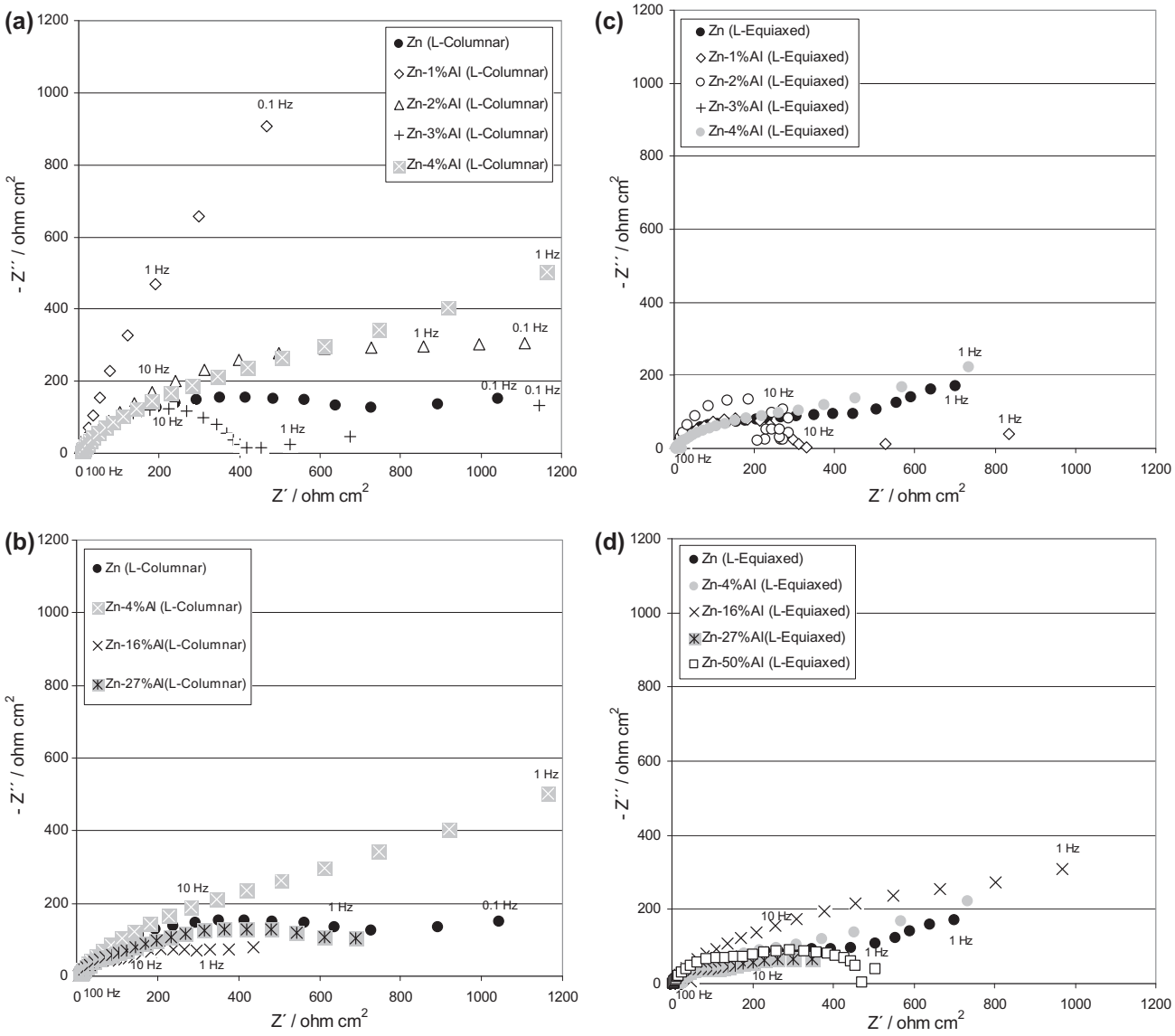

Fig. 12. Nyquist plots of (a) columnar hypoeutectic, (b) columnar hypereutectic, (c) equiaxed hypoeutectic and (d) equiaxed hypereutectic morphologies of Zn–Al alloys.

with

$$\frac{1}{Z} = \frac{1}{R_{ct} + Z_w}$$

For the hypoeutectic and hypereutectic alloys:

$$\frac{1}{Z} = \frac{1}{R_{ct} + Z_w} + jwC \qquad (2)$$

where R_Ω is the ohmic solution resistance, $\omega = 2\pi f$; C_{dl} the capacitance of the electric double layer, R_{ct} the charge transfer resistance and Z_w the diffusion contributions in impedance spectra.

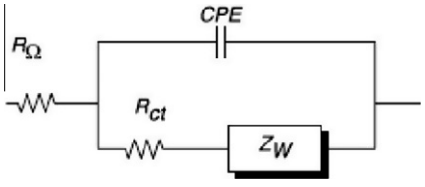

Fig. 13. Electrical equivalent circuit for modelling impedance data of Zn–Al alloys.

$Z_w = R_{DO}\ (jS)^{-05}$ for semi-infinite diffusion contribution and $Z_w = R_{DO}\ (jS)^{-05}$ coth $(jS)^{-05}$ is related to diffusion through a film of thickness d, formed on the electrode, where R_{DO} is the diffusion resistance and the parameter $S = \frac{d^2 w}{D}$, where d and D are the diffusion thickness and diffusion coefficient related to the transport process.

The good agreement between experimental and simulated data according to the transfer function given in the analysis of Eqs. (1) and (2) using non-linear least square fit routines is shown in Fig. 14.

The values of C_{dl} and R_{ct} determined from the optimum fit procedure are presented in Table 3.

The analysis of the impedance parameters associated with the time constant observed in the hypereutectic alloys at low frequencies is difficult because, this time constant is not complete in some cases. However, was possible to calculate by fitting the thickness of the films formed equal to 0.01–0.1 mm, assuming an approximate value of diffusion coefficient $D \approx 10^{-10}$ cm^2 s^{-1}.

The diameter of the first capacitive semicircle of the Nyquist plot (R_{ct}) is closely related to the corrosion rate. The value of R_{ct} could be used to calculate the corrosion current in the case of

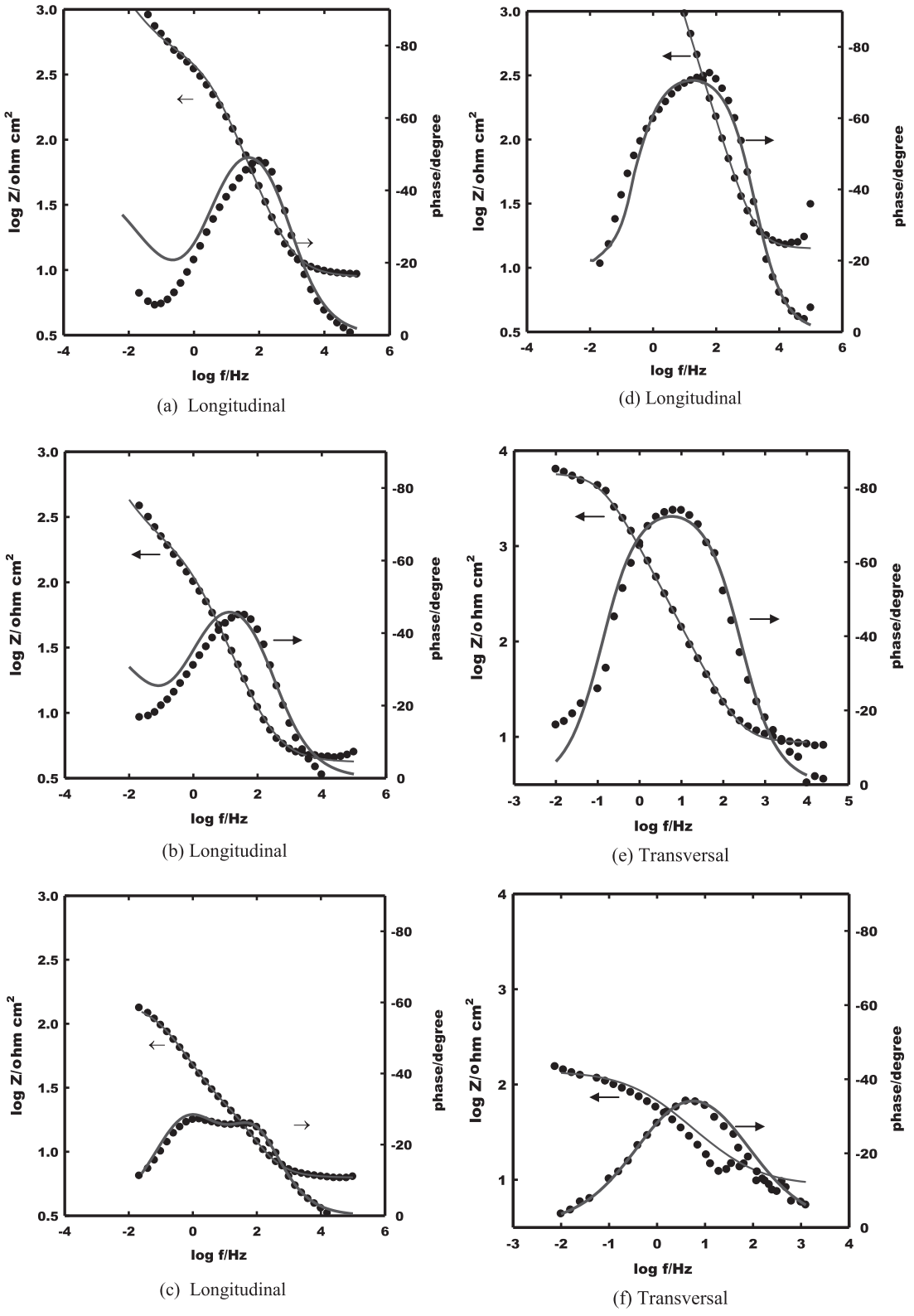

Fig. 14. Bode diagram for different alloys. (a) Zn–3 wt.%$Al_{CET\ (L)}$. (b) Zn–4 wt.%$Al_{CET\ (L)}$. (c) Zn–27 wt.%$Al_{CET\ (L)}$. (d) Al–2 wt.%$Zn_{Equiaxed\ (L)}$. (e) Al–4 wt.%$Zn_{CET\ (T)}$. (f) Zn–4 wt.%$Al_{CET\ (T)}$.

mixed control [94], where the polarization resistance technique fails, according to the following expression:

$$R_{ct} = \frac{b_a \cdot b_c}{2.303(b_a + b_c) \cdot I_{corr}} \quad (3)$$

4. Discussion

The experimental results shown in Table 3 and plotted in Fig. 15(a) demonstrate that for hypoeutectic zinc–aluminium alloys $R_{ct\ (Zn-1wt.\%Al)} > R_{ct\ (Zn-2wt.\%Al)} > R_{ct\ (Zn-3wt.\%Al)} > R_{ct\ (Zn-4wt.\%Al)}$

Table 3
Values of R_{ct} and C_{dl} determined from the optimum fit procedure.

Type of alloy and structure	R_{ct} (Ω cm^2)	C_{dl} (F cm^{-2})
$Zn_{Columnar}$	414 ± 10	$2.9 \times 10^{-4} \pm 1 \times 10^{-5}$
Zn–1 wt.%$Al_{Columnar}$	5983 ± 100	$1.9 \times 10^{-5} \pm 1 \times 10^{-6}$
Zn–1 wt.%Al_{CET}	358 ± 10	$3.0 \times 10^{-4} \pm 1 \times 10^{-5}$
Zn–1 wt.%$Al_{Equiaxed}$	310 ± 10	$2.4 \times 10^{-4} \pm 1 \times 10^{-5}$
Zn–2 wt.%$Al_{Columnar}$	800 ± 10	$1.0 \times 10^{-4} \pm 1 \times 10^{-5}$
Zn–2 wt.%Al_{CET}	503 ± 10	$2.4 \times 10^{-4} \pm 1 \times 10^{-5}$
Zn–2 wt.%$Al_{Equiaxed}$	300 ± 10	$3.2 \times 10^{-4} \pm 1 \times 10^{-5}$
Zn–3 wt.%$Al_{Columnar}$	390 ± 10	$1.3 \times 10^{-4} \pm 1 \times 10^{-5}$
Zn–3 wt.%Al_{CET}	590 ± 10	$2.1 \times 10^{-4} \pm 1 \times 10^{-5}$
Zn–3 wt.%$Al_{Equiaxed}$	234 ± 10	$3.6 \times 10^{-4} \pm 1 \times 10^{-5}$
Zn–4 wt.%$Al_{Columnar}$	551 ± 10	$8.6 \times 10^{-4} \pm 1 \times 10^{-5}$
Zn–4 wt.%Al_{CET}	345 ± 10	$1.1 \times 10^{-3} \pm 1 \times 10^{-4}$
Zn–4 wt.%$Al_{Equiaxed}$	280 ± 10	$1.7 \times 10^{-3} \pm 1 \times 10^{-4}$
Zn–16 wt.%$Al_{Columnar}$	453 ± 10	$3.8 \times 10^{-4} \pm 1 \times 10^{-5}$
Zn–16 wt.%Al_{CET}	318 ± 10	$5.3 \times 10^{-4} \pm 1 \times 10^{-5}$
Zn–16 wt.%$Al_{Equiaxed}$	220 ± 10	$2.7 \times 10^{-4} \pm 1 \times 10^{-5}$
Zn–27 wt.%$Al_{Columnar}$	390 ± 10	$3.2 \times 10^{-4} \pm 1 \times 10^{-5}$
Zn–27 wt.%Al_{CET}	300 ± 10	$4.3 \times 10^{-4} \pm 1 \times 10^{-5}$
Zn–27 wt.%$Al_{Equiaxed}$	167 ± 10	$2.3 \times 10^{-4} \pm 1 \times 10^{-5}$
Zn–50 wt.%$Al_{Columnar}$	372 ± 10	$2.2 \times 10^{-4} \pm 1 \times 10^{-5}$
Zn–50 wt.%$Al_{Equiaxed}$	153 ± 10	$1.2 \times 10^{-4} \pm 1 \times 10^{-5}$
$Al_{Columnar}$	19 ± 1	$1.9 \times 10^{-5} \pm 1 \times 10^{-6}$
Al–2 wt.%$Zn_{Equiaxed}$	11 ± 1	$2.1 \times 10^{-5} \pm 1 \times 10^{-6}$

implies that increases susceptibility to corrosion with increasing Al concentration in the inter-dendritic region (eutectic lamellar mixture).

For the hypereutectic alloys, the values of R_{ct} are slightly lower than those of the hypoeutectic alloys (Fig. 15(b)). On the other hand, also for the hypereutectic alloys the corrosion resistance decreases when the amount of aluminium increases (in the eutectic and eutectoid phases and in the β phase in the grain boundaries). This decrease in the R_{ct} values as the aluminium content increased was also found by Osório et al. [62] for Zn–25 wt.%Al and Zn 55 wt.%Al. Although Zn–4 wt.%Al is purely hypoeutectic and Zn–16 wt.%Al is purely hypereutectic, the corrosion behaviour of these alloys is intermediate, probably due to an effect of segregation of elements in the alloy.

It can be seen that, for all the compositions, the columnar morphology has higher values of R_{ct} than equiaxed, probably because columnar grains have fewer grain boundaries than equiaxed grains (Fig. 2(a)) or fewer ways for corrosion to occur, which do not have an ordered crystalline structure, and also because the grain boundaries are full of imperfections and segregation of elements.

However, it is important to note that the R_{ct} values are related to the rate of charge transfer reactions that give rise to the formation of a corrosion layer on the surface of the samples but say nothing about the protective characteristics of these films. Fig. 16 is a plot of the double-layer capacitance versus type of alloy with corresponding grain morphology (columnar, CET or equiaxed). It is possible to appreciate two different behaviours for (a) hypoeutectic and (b) hypereutectic Zn–Al alloys. In the first case, the C_{dl} increases from Zn–1 wt.%Al to Zn–4 wt.%Al, and the values for the CET zone are between those of columnar and equiaxed. In the case of Zn–4 wt.%Al, the high values of capacity confirm the formation of porous corrosion products, as determined by other authors by X-ray diffraction [46] and as shown in Fig. 11(e). These high values of capacity may also be correlated with an increase in the area.

For the hypoeutectic alloys, the C_{dl} decreases from Zn–16 wt.%Al to Zn–98 wt.%Al (Fig. 16(b)). This is consistent with the formation of small pores in the corrosion products of Fig. 11(f). The higher values of double-layer capacity are for the CET zone.

Looking at the voltammograms (Fig. 10(c) and (d)), it can be concluded that the films of corrosion products formed on alloys with higher aluminium content are more difficult to reduce. This could explain the data found in the literature reporting the beneficial effect of Al on the corrosion resistance of Zn–Al alloys [1,56,62].

The overall change in the corrosion rate of the alloys could depend on the combined influences of the changes in the aluminium

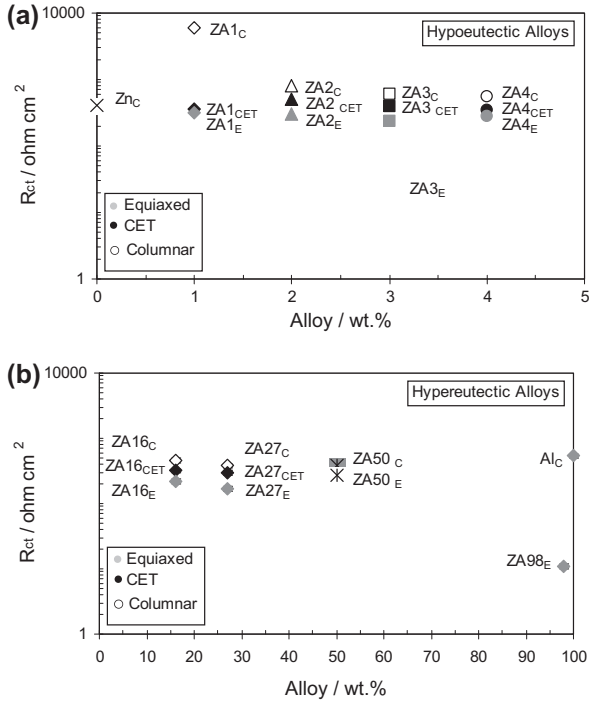

Fig. 15. Charge-transfer resistance (R_{ct}) versus type of alloy with corresponding grain morphology (columnar, CET or equiaxed) for (a) hypoeutectic and (b) hypereutectic Zn–Al alloys.

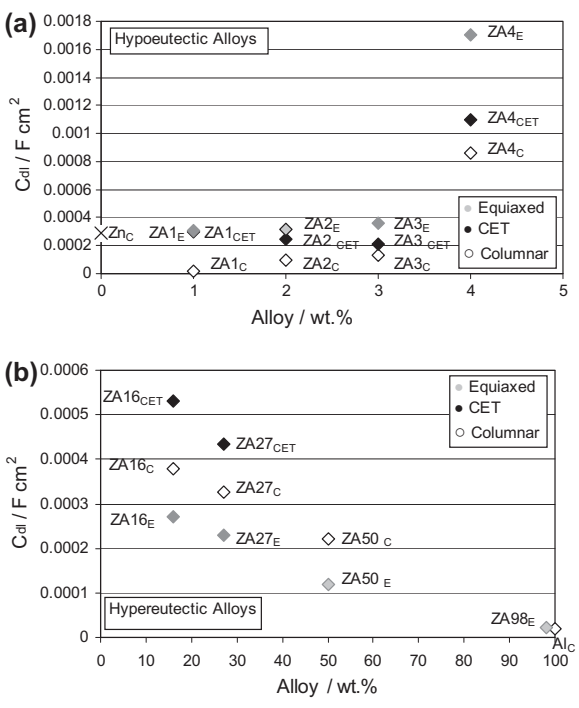

Fig. 16. Double-layer capacitance (C_{dl}) versus type of alloy with corresponding grain morphology (columnar, CET or equiaxed) for (a) hypoeutectic and (b) hypereutectic Zn–Al alloys.

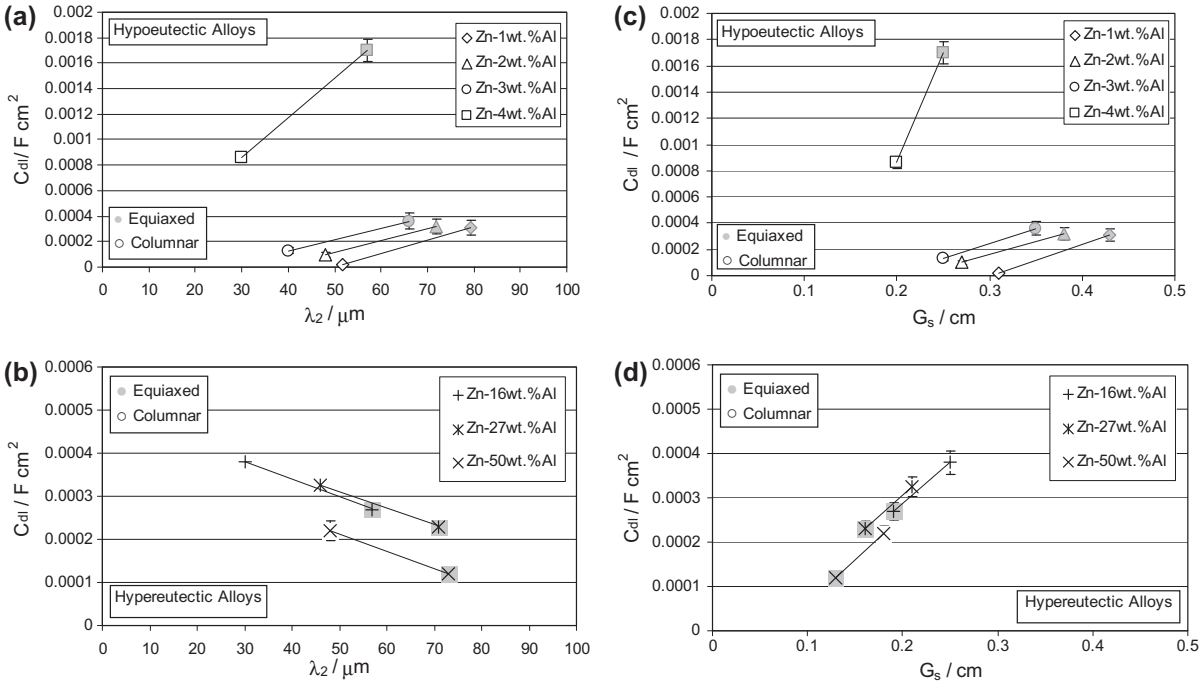

Fig. 17. Double-layer capacitance (C_{dl}) versus (a) and (b) secondary dendritic arm spacing (λ_2) and (c) and (d) grain size (G_s) for hypoeutectic and hypereutectic Zn–Al alloys.

content in the interdendritic phases and the proportion of β phase in the grain boundary.

To investigate the role of dendrite and grain morphology on corrosion resistance of hypoeutectic and hypereutectic Zn–Al alloys, we also analyzed the variation of charge-transfer resistance (R_{ct}) with secondary dendrite arm spacing (λ_2) and grain size (G_s).

Fig. 17 shows the correlation between double-layer capacitance and λ_2 and G_s. For hypoeutectic alloys, C_{dl} increases from the columnar to the equiaxed zone as both λ_2 and G_s increase (Fig. 17(a) and (c)). In contrast, for the hypereutectic alloys, C_{dl} decreases from the columnar to the equiaxed zone as λ_2 increases (Fig. 17(b)) and decreases as the G_s at the top (equiaxed zone) of the samples decreases (Fig. 17(d)).

In Fig. 18(a) and (c) for hypoeutectic alloys it possible to see that, going from the columnar to the equiaxed zones of the samples, the R_{ct} decreases as λ_2 and G_s increase. In the case of the hypereutectic alloys, the R_{ct} also decreases as λ_2 increases from the columnar to the equiaxed zone but decreases as G_s decreases.

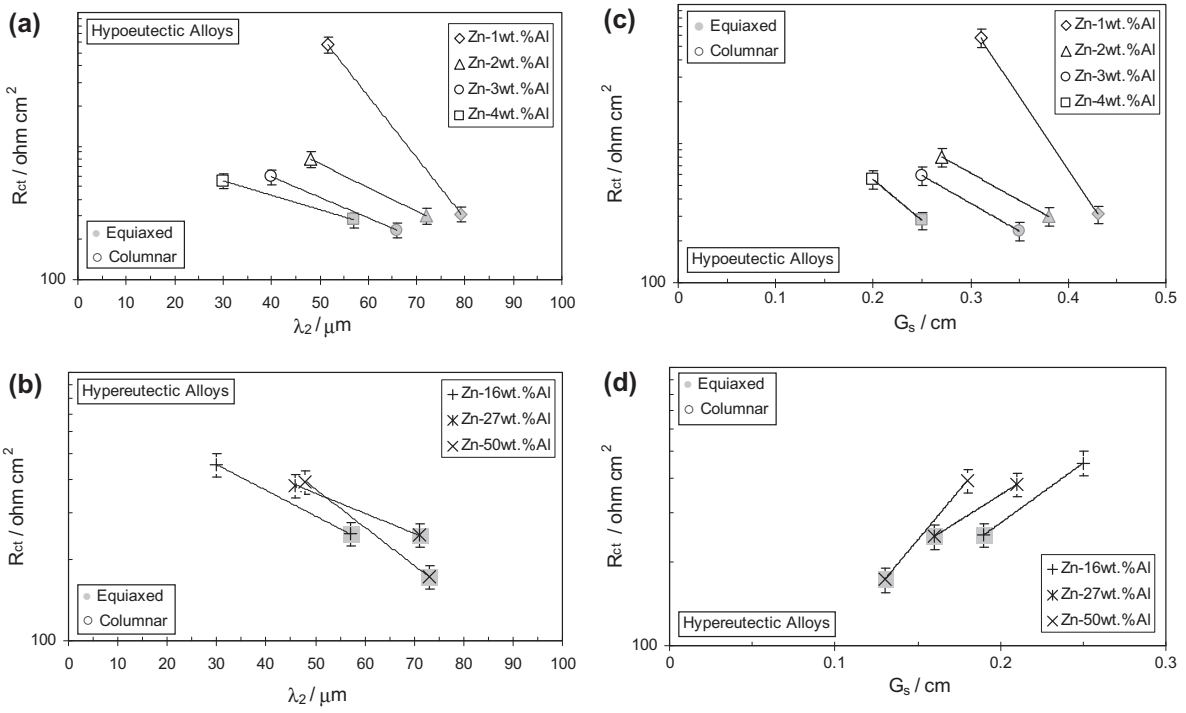

Fig. 18. Charge-transfer resistance (R_{ct}) versus (a) and (b) secondary dendritic arm spacing (λ_2) and (c) and (d) grain size (G_s) for hypoeutectic and hypereutectic Zn–Al alloys.

This means that finer dendritic microstructures tend to yield higher corrosion resistance than coarser dendritic microstructures. On the other hand, coarser columnar G_s tend to improve the corrosion resistance of hypereutectic alloys.

5. Conclusions

1. Using the electrochemical impedance spectroscopy (EIS) technique allowed us to evaluate the corrosion behaviour of different Zn–Al alloys in a 3% NaCl solution.
2. The corrosion resistance is a complex function of the alloy composition, macrostructure and microstructure and section of the samples, all of which determine the protective characteristics of the films that are formed on them.
3. The values of the charge-transfer resistance were used as a basic criterion for the evaluation of the corrosion resistance of the alloys, but do not indicate the protective properties of the films formed on the Zn–Al alloys directionally solidified.
4. It can be seen that, for all the compositions, the columnar morphology has higher values of charge-transfer resistance than equiaxed, probably because columnar grains have fewer grain boundaries and imperfections than equiaxed grains.
5. Although the value of charge-transfer resistance decreases as the aluminium concentration increases, the films formed at higher concentrations of aluminium appear to be more protective since they cannot be reduced during the cathodic sweep in voltammetry.
6. The control of microstructure can be used to produce alloys with better corrosion resistance.
7. This research shows that what actually affects the response to corrosion is the way in which aluminium is distributed in the alloy, i.e., which phases are present in the solidified microstructure and how they are distributed, and not the amount of aluminium present in the alloy.

Acknowledgements

We wish to thank the Centro Atómico Constituyentes (Comisión Nacional de Energía Atómica) from Argentina for the scanning microscopy facilities.

We also acknowledge the financial support of the Consejo Nacional de Investigaciones Científicas y Técnicas (CONICET) and the Agencia Nacional de Promoción Científica y Tecnológica (ANPCyT) of Argentina.

References

[1] X.G. Zhang, Corrosion and Electrochemistry of Zinc, Plenum Press, New York and London, 1996.
[2] R.J. Barnhurst, S. Beliste, Corrosion Properties of Zamak and ZA Alloys, Noranda Technology Centre, Quebec, Canada, 1992.
[3] E.J. Kubel, Advanced materials and processes inc, Met. Prog. 7 (1987) 51–57.
[4] C. Cachet, C.P. De Pauli, R. Wiart, The passivation of zinc in slightly alkaline solutions, Corros. Sci. 25 (1985) 493–502.
[5] A. Jardy, R. Rosset, R. Wiart, Diphosphate coatings for protection of galvanized steel: quality control by impedance measurements, J. Appl. Electrochem. 14 (1984) 537–545.
[6] C. Deslouis, M. Duprat, Chr. Tournillon, The kinetics of zinc dissolution in aerated sodium sulphate solutions, a measurement of the corrosion rate by impedance techniques, Corros. Sci. 29 (1989) 13–30.
[7] L.M. Baugh, Corrosion and polarization characteristics of zinc in neutral-acid media. Part I. Pure zinc in solutions of various sodium salts, Electrochim. Acta 24 (1979) 657–667.
[8] F. Mansfeld, S. Gilman, The effect of several electrode and electrolyte additives on the corrosion and polarisation behaviour of the alkaline zinc electrode, J. Electrochem. Soc. 117 (1970) 1328–1333.
[9] M. Dattilo, Polarization and corrosion of electrogalvanized steel-evaluation of zinc coating obtained from waste-derived zinc electrolytes, J. Electrochem. Soc. 132 (1985) 2557–2561.
[10] H. Leidheiser, G.W. Simmons, S. Nagy, S. Music, Mossbauer spectroscopic study of the corrosion inhibition of zinc by cobalt ions, J. Electrochem. Soc. 129 (1982) 1658–1662.
[11] L.M. Baugh, Corrosion and polarization characteristics of zinc in neutral-acid media. Part II. Effect of NH_4^+ ions and the role of battery zinc alloying constituents, Electrochim. Acta 24 (1979) 669–677.
[12] T. Yamashita, Electro-deposition and electro-dissolution of zinc in the vicinity of equilibrium potential in aqueous zinc sulphate solutions, J. Electroanal. Chem. Interfacial Electrochem. 106 (1980) 95–102.
[13] N. Bocchi, C.V. D'Alkaine, Zinc behavior in slightly alkaline solutions. The reduction processes, Key Eng. Mater. 20–28 (1988) 417–423.
[14] D.A. Jones, N.R. Nair, Electrochemical corrosion studies on zinc-coated steels, Corrosion 41 (1985) 357–362.
[15] M. Nòvak, S. Szues, Study of electropolishing of a Zn anode in acidic medium, J. Electroanal. Chem. Interfacial Electrochem. 266 (1989) 157–172.
[16] C. De Pauli, O.A.H. Derosa, M.C. Giordano, Effect of phosphate ions on zinc dissolution in alkaline solutions, J. Electroanal. Chem. Interfacial Electrochem. 73 (1976) 105–108.
[17] R. Wiart, C. Cachet, C. Bozhkov, S. Rashkov, On the nature of the "induction period" during the electrowinning of zinc from nickel containing sulphate electrolytes, J. Appl. Electrochem. 20 (1990) 381–389.
[18] H.S. Wroblowa, S.B. Qaderi, The mechanism of oxygen reduction on zinc, J. Electroanal. Chem. Interfacial Electrochem. 295 (1990) 153–161.
[19] A.E. Bothe, J.R. Vilche, K. Jüttner, W.J. Lorenz, W. Kautek, W. Paatchsch, An electrochemical impedance spectroscopy study of passive zinc and low alloyed zinc electrodes in alkaline and neutral aqueous solutions, Corros. Sci. 32 (1991) 621–633.
[20] P.L. Cabot, M. Cortes, F.A. Centellas, J.A. Garrido, E. Perez, Potentiodynamic passivation of zinc in aqueous KOH solutions, J. Electroanal. Chem. Interfacial Electrochem. 201 (1986) 85–100.
[21] M.W. Breiter, Dissolution and passivation of vertical porous zinc electrodes in alkaline solution, Electrochim. Acta 15 (1970) 1297–1304.
[22] M.S. Abdel-Aal, Z.A. Ahmed, M.S. Hassan, Inhibiting and accelerating effects of some quinolines on the corrosion of zinc and some binary zinc alloys in HCl solution, J. Appl. Electrochem. 22 (1992) 1104–1109.
[23] V.S. Muralidharan, K.S. Rajagopalan, Kinetics and mechanism of corrosion of zinc in sodium hydroxide solutions by steady-state and transient methods, J. Electroanal. Chem. Interfacial Electrochem. 94 (1978) 21–36.
[24] I. Epelboin, M. Ksouri, R. Wiart, On a model for the electrocrystallization of zinc involving an autocatalytic step, J. Electrochem. Soc. 122 (1975) 1206–1214.
[25] J.W. Johnson, Y.C. Sun, W.J. James, Anodic dissolution of Zn in aqueous salt solutions, Corros. Sci. 11 (1971) 153–159.
[26] C. Cachet, U. Stroder, R. Wiart, The kinetics of zinc electrode in alkaline zincate electrolytes, Electrochim. Acta 27 (1982) 903–908.
[27] C. Deslouis, M. Duprat, C. Tulet-Tournillon, The cathodic mass transport process during zinc corrosion in neutral aerated sodium sulphate solutions, J. Electroanal. Chem. Interfacial Electrochem. 181 (1984) 119–136.
[28] C. Cachet, R. Wiart, Zinc deposition and passivation hydrogen evolution in highly acidic sulphate electrolytes, depassivation by nickel impurities, J. Appl. Electrochem. 20 (1990) 1009–1014.
[29] R.D. Armstrong, M.F. Bell, The active dissolution of zinc in alkaline solution, Electroanal. Chem. Interfacial Electrochem. 55 (1974) 201–211.
[30] T. Hurlen, K.P. Fisher, Kinetics of Zn/Zn(II) reactions in acidified solutions of potassium chloride, Electoanal. Chem. Interfacial Electrochem. 61 (1975) 165–173.
[31] T.P. Dirkse, Voltage decay at passivated zinc anodes, J. Appl. Electrochem. 1 (1971) 27–33.
[32] K.G. Boto, L.F.G. Williams, The determination of the corrosion rate of zinc in solution by the differential pulse method, J. Electrochem. Soc. 124 (1977) 656–661.
[33] J.O.M. Bockris, Z. Nagy, A. Damjanovic, On the deposition and dissolution of zinc in alkaline solutions, J. Electrochem. Soc. 119 (1972) 285–295.
[34] M. Liu, G.M. Cook, N.P. Yao, Passivation of zinc anodes in KOH electrolytes, J. Electrochem. Soc. 128 (1981) 1663–1668.
[35] P.L. Cabot, M. Cortes, F. Centellas, E. Peres, Potentiostatic passivation of zinc in alkaline solutions, J. Appl. Electrochem. 23 (1993) 371–378.
[36] G.W. Walter, Corrosion rates of zinc, zinc coatings, and steel in aerated slightly acidic chloride solutions calculated from low polarization data, Corros. Sci. 16 (1976) 573–586.
[37] N.A. Hampson, G.A. Herdman, R. Taylor, Some kinetic and thermodynamic studies of the system Zn/Zn(II), OH^-, J. Electroanal. Chem. Interfacial Electrochem. 25 (1970) 9–18.
[38] T.P. Dirkse, N.A. Hampson, The Zn(II)/Zn exchange reaction in KOH solution. Part II. Exchange current density measurements using the double-impulse method, Electrochim. Acta 17 (1972) 383–386.
[39] T.S. Lee, Hydrogen overpotential on pure metals in alkaline solution, J. Electrochem. Soc. 118 (1971) 1278–1282.
[40] T.S. Lee, Hydrogen overpotential on zinc alloys in alkaline solution, J. Electrochem. Soc. 122 (1975) 171–173.
[41] Z. Zembura, L. Burzynska, The corrosion of zinc in de-aerated 0.1 M NaCl in the pH range from 1.6 to 13.3, Corros. Sci. 17 (1977) 871–878.
[42] K.G. Boto, L.F.G. Williams, Rotating disc electrode studies of zinc corrosion, J. Electroanal. Chem. Interfacial Electrochem. 77 (1977) 1–20.
[43] A.D. Davydov, T.B. Zhukova, G.R. Engelgardt, Concentration changes in the solution layer next to the anode and the maximum current of electrochemical zinc dissolution in alkalies, Russ. J. Electrochem. 26 (1990) 1207–1209.

[44] K. Schwabe, H.B. Luck, The anodic behavior of zinc in saturated solution of zinc sulphate, Electrochim. Acta 17 (1972) 99–105.
[45] M. Gmytryk, J. Sedzimir, Corrosion of Zn in deaerated sulphate solutions at different pH values, Corros. Sci. 7 (1967) 683–695.
[46] L. Fedrizzi, L. Ciaghi, P.L. Bonora, R. Fratesi, G. Roventi, Corrosion behaviour of electrogalvanized steel in sodium chloride and ammonium sulphate solutions, a study by EIS, J. Appl. Electrochem. 22 (1992) 247–254.
[47] T. Hurlen, Kinetics of metal/metal-ion electrodes: iron, copper, zinc, Electrochim. Acta 7 (1962) 653–668.
[48] H. Park, J.A. Szpunar, The role of texture and morphology in optimizing the corrosion resistance of zinc-based electrogalvanized coatings, Corros. Sci. 40 (1995) 525–545.
[49] K.G. Watkins, M.A. McMahon, W.M. Steen, Microstructure and corrosion properties of laser surface processed aluminium alloys: a review, Mater. Sci. Eng. A 231 (1997) 55–61.
[50] G.Y. Liang, T.T. Wong, Microstructure and character of laser remelting of plasma sprayed coating (Ni–Cr–B–Si) on Al–Si alloy, Surf. Coat. Technol. 89 (1997) 121–126.
[51] J.K. Shin, J.H. Suh, J.S. Kim, S.J.L. Kang, Effect of laser surface modification on the corrosion resistance of alloy 600, Surf. Coat. Technol. 107 (1998) 94–100.
[52] I. García, J.J. De Damborenea, Corrosion properties of tin prepared by laser gas alloying of Ti and Ti–6Al–4V, Corros. Sci. 40 (1998) 1411–1419.
[53] A. Conde, R. Colaço, R. Vilar, J. De Damborenea, Corrosion behaviour of steels after laser surface melting, Mater. Des. 21 (2000) 441–445.
[54] F. Torster, G. Baumeister, J. Albrecht, G. Lutjering, D. Helm, M.A. Daeubler, Influence of grain size and heat treatment on the microstructure and mechanical properties of the nickel-base superalloy U720LI, Mater. Sci. Eng. A 234–236 (1997) 189–192.
[55] G. Song, A. Atrens, M. Dareusch, Influence of microstructure on the corrosion of diecast AZ91D, Corr. Sci. 41 (1999) 249–273.
[56] G. Song, A.L. Bowles, D.H. St. John, Corrosion resistance of aged die cast magnesium alloy AZ91D, Mater. Sci. Eng. A 366 (2004) 74–86.
[57] T.M. Yue, L.J. Yan, C.P. Chan, C.F. Dong, H.C. Man, G.K.H. Pang, Excimer laser surface treatment of aluminum alloy AA7075 to improve corrosion resistance, Surf. Coat. Technol. 179 (2004) 158–164.
[58] E. Barsoukov, J. Ross McDonald, Impedance Spectroscopy. Theory, Experiment and Applications, John, Wiley & Sons, Inc., Hoboken, New Jersey and Canada, 2005.
[59] J.A. Spittle, Columnar to equiaxed grain transition in as solidified alloys, Int. Mater. Rev. 51 (2006) 247–269.
[60] W.R. Osório, M.E.P. Souza, C.M. Freire, A. Garcia, The application of electrochemical impedance spectroscopy to investigate the effect of as-cast structures on the corrosion resistance of hypereutectic Zn–Al alloys, J. New Mater. Electrochem. Syst. 11 (2008) 37–42.
[61] W.R. Osório, C.M. Freire, A. Garcia, The role of macrostructural morphology and grain size on the corrosion resistance of Zn and Al castings, Mater. Sci. Eng. A 402 (2005) 22–32.
[62] W.R. Osório, C.M. Freire, A. Garcia, The effect of the dendritic microstructure on the corrosion resistance of Zn–Al alloys, J. Alloy. Compd. 397 (2005) 179–191.
[63] A.E. Ares, L.M. Gassa, S.F. Gueijman, C.E. Schvezov, Correlation between thermal parameters, structures, dendritic spacing and corrosion behavior of Zn–Al alloys with columnar to equiaxed transition, J. Cryst. Growth 310 (2008) 1355–1361.
[64] T. Watanabe, An approach to grain boundary design for strong and ductile polycrystals, Res. Mech. 11 (1984) 47–84.
[65] G. Schikorr, I. Schikorr, The resistance of zinc to atmospheric corrosion, Z. Metallkd. 35 (1943) 175–181.
[66] E. von Riecke, Investigation on the influence of zinc on the corrosion behavior of high strength steels, Werkst. Korros. 30 (1979) 619–630.
[67] D.J. Wills, A. De Lisen, B. Glecson, Intergranular corrosion in continuosly galvanized steels, Galvatech '95, Iron and Steel Society, Chicago, 1995.
[68] J.R. Sarazin, A. Hellawell, A channel formation in Pb–Sn–Sb alloys ingots and comparison with the system NH_4Cl–H_2O, Metall. Mater. Trans. A 19 (1988) 1861–1871.
[69] S.N. Tewari, R. Shah, Macrosegregation during dendritic arrayed growth of hypoeutectic Pb–Sn alloys, Metall. Mater. Trans. A 27 (1996) 1353–1362.
[70] T.M. Pollock, W.H. Murphy, The breakdown of single-crystal solidification in high refractory nickel-base alloys, Metall. Mater. Trans. A 27 (1996) 1081–1094.
[71] S.H. Han, R. Trivedi, Primary spacing selection in directionally solidification alloys, Acta Metall. Mater. 42 (1994) 25–41.
[72] H. Kim, J.C. Earthman, E.J. Lavernia, Directional solidification of Ni_3Al, Acta Metall. Mater. 40 (1992) 637–647.
[73] D. Bourchard, J.S. Kirkaldy, Prediction of dendrite arm spacings in unsteady- and steady-state heat flow of unidirectionally solidified binary alloys, Metall. Mater. Trans. B 28 (1997) 651–663.
[74] D. Ma, P. Sahm, Primary spacing in directional solidification, Metall. Mater. Trans. A 29 (1998) 1113–1119.
[75] S.H. Han, R. Trivedi, Primary spacing selection in directionally solidified alloys, Acta Metall. Mater. 42 (1994) 25–41.
[76] Y.L. Liu, S.B. Kang, Solidification and segregation of Al–Mg alloys and influence of alloy composition and cooling rate, Mater. Sci. Technol. 13 (1997) 331–336.
[77] K. Cruz, J. Spinelli, I. Ferreira, N. Cheung, A. Garcia, Microstructural development in Al–Sn alloys directionally solidified under transient heat flow conditions, Mater. Chem. Phys. 109 (2008) 87–98.
[78] W. Kurz, D.J. Fisher, Fundamentals of Solidification, Trans. Tech. Publications, Switzerland, 1992.
[79] J.S. Langer, H. Muller-Krumbhaar, Stability effects in dendritic crystal growth, J. Crystal Growth 42 (1977) 11–14.
[80] N.J. Petch, The cleavage strength of polycrystals, J. Iron Steel Inst. 174 (1953) 25–28.
[81] P. Donelan, Modelling microstructural and mechanical properties of ferritic ductile cast iron, Mater. Sci. Technol. 16 (2000) 261–269.
[82] J. Campbell, Castings, second ed., Butterworth-Heinemann, Oxford, United Kingdom, 1991.
[83] W.R. Osório, A. Garcia, Modeling dendritic structure and mechanical properties of Zn–Al alloys as a function of solidification conditions, Mater. Sci. Eng. A 325 (2002) 103–111.
[84] W.R. Osório, C.A. Santos, J.M.V. Quaresma, A. Garcia, Mechanical properties as a function of thermal parameters and microstructure of Zn–Al castings, J. Mater. Proc. Technol. 143 (2003) 703–709.
[85] J.M.W. Quaresma, C.A. Santos, A. Garcia, Correlation between unsteady-state solidification conditions, dendrite spacings, and mechanical properties of Al–Cu alloys, Metall. Mater. Trans. A 31 (2000) 3167–3178.
[86] A.E. Ares, C.E. Schvezov, The effect of structure on tensile properties of directionally solidified Zn-based alloys, J. Cryst. Growth 318 (2011) 59–65.
[87] A.E. Ares, C.E. Schvezov, Influence of solidification thermal parameters on the columnar to equiaxed transition of aluminum–zinc and zinc–aluminum alloys, Metall. Mater. Trans. 38 A (2007) 1485–1499.
[88] G.F. Vander Voort, Metallography Principles and Practice, ASM International, 1999.
[89] H.E. Boyer, T.L. Gall, Metals Handbook, Desk ed., American Society for Metals, USA, 1990.
[90] L.J. Kotnik An Investigation of the Properties of Zinc Corrosion Products, Ph.D. Thesis, Case Institute of Technology, 1960.
[91] J. Augustynski, Etude de la rupture de passivite de certains metaux electrochimiquement actifs, Corros. Sci. 13 (1978) 955–965.
[92] H. Morrow, in: M.B. Bever (Ed.), Encyclopedia of Materials Science and Engineering, vol. 7, MIT Press, Cambridge, Massachusetts, 1986.
[93] G. Trabanelli, F. Zucchi, G. Brunoro, G. Gilli, Characterization of the corrosion or anodic oxidation products on zinc, Electrodepos. Surf. Treat. 3 (1975) 129–138.
[94] I. Epelboin, M. Keddam, H. Takenouti, Use of impedance measurements for the determination of the instant rate of metal corrosion, J. Appl. Electrochem. 2 (1972) 71–79.